



AMERICAN METEOROLOGICAL SOCIETY

Journal of the Atmospheric Sciences

EARLY ONLINE RELEASE

This is a preliminary PDF of the author-produced manuscript that has been peer-reviewed and accepted for publication. Since it is being posted so soon after acceptance, it has not yet been copyedited, formatted, or processed by AMS Publications. This preliminary version of the manuscript may be downloaded, distributed, and cited, but please be aware that there will be visual differences and possibly some content differences between this version and the final published version.

The DOI for this manuscript is doi: 10.1175/JAS-D-14-0202.1

The final published version of this manuscript will replace the preliminary version at the above DOI once it is available.

If you would like to cite this EOR in a separate work, please use the following full citation:

Johnson, R., P. Ciesielski, J. Ruppert, Jr., and M. Katsumata, 2014: Sounding-Based Thermodynamic Budgets for DYNAMO. *J. Atmos. Sci.* doi:10.1175/JAS-D-14-0202.1, in press.



Sounding-Based Thermodynamic Budgets for DYNAMO

Richard H. Johnson*, Paul E. Ciesielski, and James H. Ruppert, Jr.

Colorado State University, Fort Collins, Colorado

Masaki Katsumata

Research Institute for Global Change, Japan Agency for Marine-Earth Science and Technology,

Yokosuka, Japan

PRELIMINARY ACCEPTED VERSION

*Corresponding author address: Department of Atmospheric Science, Colorado State University

E-mail: johnson@atmos.colostate.edu

ABSTRACT

3 The DYNAMO (Dynamics of the MJO) field campaign, conducted over the
4 Indian Ocean from October 2011 to March 2012, was designed to study the
5 initiation of the Madden-Julian Oscillation (MJO). Two prominent MJOs oc-
6 curred in the experimental domain during the Special Observing Period in
7 October and November. Data from a northern and a southern sounding array
8 (NSA and SSA, respectively) have been used to investigate the apparent heat
9 sources and sinks (Q_1 and Q_2) and radiative heating rates Q_R throughout the
10 life cycles of the two MJO events. The MJO signal was far stronger in the
11 NSA than the SSA. Time series of Q_1 , Q_2 , and the vertical eddy flux of moist
12 static energy reveal an evolution of cloud systems for both MJOs consistent
13 with prior studies: shallow, non-precipitating cumulus during the suppressed
14 phase, followed by cumulus congestus, then deep convection during the ac-
15 tive phase, and finally stratiform precipitation. However, the duration of these
16 phases was shorter for the November MJO than for the October event. The
17 profiles of Q_1 and Q_2 for the two arrays indicate a greater stratiform rain frac-
18 tion for the NSA than the SSA, a finding supported by TRMM measurements.
19 Surface rainfall rates and net-tropospheric Q_R determined as residuals from
20 the budgets show good agreement with satellite-based estimates. The cloud
21 radiative forcing was approximately 20% of the column-integrated convec-
22 tive heating and of the same magnitude as the normalized gross moist stabil-
23 ity, leaving open the possibility of radiative-convective instability for the two
24 MJOs.

3 **1. Introduction**

4 The Madden-Julian Oscillation (MJO; Madden and Julian 1972) is one of the most prominent
5 features of the general circulation, having global impacts on weather and climate (Zhang 2013).
6 Despite the considerable attention given to the MJO in recent years, there remain significant gaps
7 in understanding and prediction of the phenomenon (Hung et al. 2013; Zhang et al. 2013). A field
8 campaign was conducted over the Indian Ocean from October 2011 to March 2012 to investigate
9 a number of the outstanding issues related to the MJO, with particular attention to tropospheric
10 moistening processes, evolving cloud populations, and air-sea interaction during its initiation. The
11 experiment consisted of four collaborating campaign components (Yoneyama et al. 2013): DY-
12 NAMO (Dynamics of the MJO); CINDY (Cooperative Indian Ocean experiment on intraseasonal
13 variability in the Year 2011); AMIE (ARM MJO Investigation Experiment); and LASP (Littoral
14 Air-Sea Processes). Hereafter, we will refer to the combined effort as DYNAMO.

15 Emerging from MJO studies over the past several decades is the concept of a distinct, repeatable
16 evolution of precipitation systems within the MJO convective envelope. Namely, cloud popula-
17 tions through the MJO life cycle have been observed where the dominant mode of convection
18 transitions from shallow cumulus to cumulus congestus to deep convection to stratiform precip-
19 itation systems (Johnson et al. 1999; Kikuchi and Takayabu 2004; Benedict and Randall 2007;
20 Haertel et al. 2008; Del Genio et al. 2012; Xu and Rutledge 2014). This pattern of evolution is
21 found to occur over a wide range of time and space scales and associated with a variety of tropical
22 disturbances, ranging from individual convective systems to the MJO itself (Kiladis et al. 2005,
23 2009). Within the framework of the MJO, the pattern is characterized by changing frequency
24 distributions of cloud types through the overall life cycle rather than one cloud type existing in
25 each MJO phase, supportive of the “building block” hypothesis proposed by Mapes et al. (2006).

26 Moreover, there is evidence from the studies of Kikuchi and Takayabu (2004), Yoneyama et al.
27 (2008), Virts and Wallace (2010), Del Genio et al. (2012), and Johnson and Ciesielski (2013) to
28 indicate that the progression of the cloud population in the build-up phase of the MJO actually
29 occurs in a stepwise fashion, with distinct periods of \sim week or more when there is a dominance
30 of each (cumulus, congestus, cumulonimbus) cloud type. However, the mechanisms by which the
31 atmosphere is moistened during the initiation phase of the MJO are still not well understood and
32 remain a matter of considerable debate (e.g., Waite and Khouider 2010; Hohenegger and Stevens
33 2013; Barnes and Houze 2013; Powell and Houze 2013; Yuan and Houze 2013).

34 DYNAMO was designed to explore moistening processes and cloud populations within the MJO
35 using multiple instrument platforms: cloud and precipitation radars, profilers, sounding networks,
36 aircraft, and satellites. This study focuses primarily on one aspect of the DYNAMO measurement
37 system – the sounding network – to compute heat and moisture budgets following the procedures
38 of Yanai et al. (1973), with the goal of inferring properties of convective systems and their roles
39 of latent heating and moistening/drying within the MJO. While there have been numerous studies
40 investigating diabatic heating in the MJO using reanalysis data (for a review, see Zhang et al.
41 2013), model-independent computations of MJO heating profiles from field campaigns are limited.

42 The first opportunity to directly compute heating profiles and moistening processes within the
43 MJO using a network of soundings was for the 1992-93 TOGA COARE (Tropical Ocean Global
44 Atmosphere Coupled Atmosphere-Ocean Response Experiment; Webster and Lukas 1992). These
45 studies revealed a population of cloud systems within the MJO, progressing from shallow cumu-
46 lus, to congestus, to deep convection to stratiform through the life cycle (Lin and Johnson 1996;
47 Johnson and Lin 1987; Johnson et al. 1999; Tung et al. 1999). Diabatic heating profiles were also
48 determined for the 2006 MISMO (Mirai Indian Ocean cruise for the Study of the Madden-Julian
49 oscillation (MJO)-convection Onset; Yoneyama et al. 2008). Katsumata et al. (2011) found pro-

50 files of apparent heat source Q_1 and apparent moisture sink Q_2 during MISMO for an abortive
51 MJO similar to those for TOGA COARE.

52 DYNAMO affords a third opportunity to investigate heating and moistening within the MJO, but
53 this time with improved sounding instrumentation compared to TOGA COARE (Ciesielski et al.
54 2014a) and with higher time-resolution launches (most sites in the core DYNAMO domain had
55 three-hourly soundings as opposed to six-hourly in TOGA COARE). In this study, we compute the
56 apparent heat source Q_1 and apparent moisture sink Q_2 of Yanai et al. (1973) for the DYNAMO
57 sounding arrays and combine the results with independent estimates of surface fluxes to compute
58 surface precipitation and net-tropospheric radiative heating rates for the months of October and
59 November 2011. Two prominent MJO events occurred during this period (Gottschalck et al. 2013;
60 Yoneyama et al. 2013; Johnson and Ciesielski 2013). The findings are then compared to satellite-
61 based estimates of those quantities. The DYNAMO sounding array analyses have already formed
62 the basis for large-scale forcing fields being used by various authors, so evaluation of the accu-
63 racy of those analyses through comparison with independent estimates is important. The analysis
64 products developed in this study have been recently used by Sobel et al. (2014) to investigate the
65 moist static energy budget for the DYNAMO MJOs.

66 Observations collected on Gan Island during AMIE have enabled the computation of the vertical
67 profile of radiative heating in the troposphere at that location as a function of time throughout the
68 experiment (Feng et al. 2014). We use these estimates of the radiative heating profile to determine
69 time series of the vertical flux of moist static energy, which provides a measure of cumulus ac-
70 tivity (Yanai et al. 1973). This information, along with the fields of Q_1 and Q_2 , will be used to
71 infer characteristics of the evolving cloud populations during the DYNAMO MJOs. In addition,
72 the possible role of radiative-convective instability in the MJO (Yu et al. 1998; Raymond 2001;
73 Stephens et al. 2004; Lin and Mapes 2004; Jiang et al. 2011) will be explored based on computa-

74 tions of column-integrated radiative and convective heating rates for the two MJOs and comparing
75 them to the normalized gross moist stability (Neelin and Held 1997; Raymond et al. 2009; Sobel
76 and Maloney 2012, 2013). Further work is underway to relate the budget results to cloud popu-
77 lations as determined by the research radars, but that effort is awaiting additional quality control
78 and evaluation of the radar products.

79 **2. Data and analysis procedures**

80 *a. Sounding observations*

81 The DYNAMO sounding network was composed of two quadrilateral arrays, one north and
82 one south of the equator, referred to as the Northern and Southern Sounding Arrays or NSA and
83 SSA, respectively (Fig. 1). Details of the sounding systems, observing characteristics, and quality-
84 control procedures are contained in Ciesielski et al. (2014a). Incorporated into our analyses are
85 corrections for flow distortion and island heating effects by the mountainous island of Sri Lanka
86 on Colombo soundings (Ciesielski et al. 2014b). Blockage of the low-level flow by the island
87 terrain frequently disrupts the winds at Colombo below about 2 km. This local effect is aliased
88 onto larger scales and impairs computations of divergence over the NSA. The procedure developed
89 by Ciesielski et al. (2014b) mitigates the impacts of Sri Lanka flow blocking on budgets over the
90 NSA by using ECMWF Operational Analysis (OA) data away from the island to estimate what
91 the wind, temperature, and moisture would be in the lowest 2 km at Colombo were the island not
92 present.

93 The previous study of the thermodynamic and kinematic fields during the DYNAMO Special
94 Observing Period or SOP (October and November 2011) by Johnson and Ciesielski (2013) was
95 based on a preliminary version of the sounding data, which did not include corrections for humidity

96 sensor biases at all sites. This study uses the complete set of corrections for humidity biases based
97 on procedures described in Ciesielski et al. (2014a). In DYNAMO, Vaisala RS92 systems were
98 used at five of the six SSA and NSA sites, while Colombo used a Meisei system. The humidity
99 biases for the RS92s have been found to be relatively small, namely, daytime dry biases of $\sim 2\%$ in
100 the lower troposphere and 5-6% in the upper troposphere, which are only a third of the magnitude
101 of the biases for the Vaisala RS80 sensors used in TOGA COARE (Wang et al. 2002; Ciesielski
102 et al. 2003).

103 In addition to upsonde data, dropsonde data from the National Oceanic and Atmospheric Ad-
104 ministration (NOAA) P-3 aircraft were incorporated into the gridded analyses described below.
105 There were 469 dropsonde observations from thirteen flights in proximity to the sounding arrays
106 during the period 9 November-13 December.

107 To supplement conventional sounding winds, two sources of satellite winds were employed.
108 First, surface winds over the ocean were obtained from the Advanced Scatterometer (ASCAT)
109 on the MetOP-A satellite, which provides wind estimates nominally twice per day (3-6 UTC and
110 15-18 UTC over the Indian Ocean) on a 12.5-km grid (Figa-Saldaña et al. 2002). To facilitate
111 their use in our objective analysis, non-rain contaminated Level 2 ASCAT winds were averaged
112 into 3-h, 2.5° bins. In addition to these surface winds, we utilized upper-level atmospheric motion
113 vector data derived from Meteosat-7 visible, infrared and water vapor data (Holmlund et al. 2001)
114 produced by the Cooperative Institute of Meteorological Studies (CIMSS). For our analysis, these
115 hourly wind vectors were averaged into 3-h, 25-hPa, 5° -resolution bins and used, only if at least
116 three high-quality wind observations were present in a given bin. With this criterion, averaged
117 satellite winds over the central Indian Ocean were available at 5° resolution $>80\%$ of the time for
118 levels between 300 and 175 hPa and $\sim 20\%$ of the time for levels between 825 and 775 hPa with
119 few observations at other levels.

120 Sounding thermodynamic data were supplemented with radio occultation (RO) profiles of T and
121 T_d from the COSMIC wetPrf product based on a 1-D variational analysis using ECMWF analysis
122 as a first guess (Kuo et al. 2004). There were approximately ten COSMIC profiles per month over
123 each $5^\circ \times 5^\circ$ box over the Indian Ocean. Because of the well-documented negative refractivity
124 bias in the tropical lower-troposphere of RO soundings (Ao et al. 2003), no T_d information from
125 this product was used below 850 hPa.

126 *b. Other data sources*

127 Precipitation rates derived from the sounding budgets are compared to estimates from several
128 different sources. One is the TRMM (Tropical Rainfall Measuring Mission) 3B42v7 product,
129 which combines microwave rainfall estimates from TRMM and other satellites with high temporal
130 resolution infrared rain rate estimates to create a 3-hourly, $0.25^\circ \times 0.25^\circ$ rainfall data set (Huff-
131 man et al. 2007). Other sources are the NOAA CPC Morphing Technique or CMORPH (Joyce
132 et al. 2004), available on a 0.07° grid and at 30-min time resolution; the Global Precipitation Cli-
133 matology Project (GPCP) with daily values on a 0.25° grid (Adler et al. 2003); and the Global
134 Satellite Mapping of Precipitation (GSMaP) with hourly values on a 0.10° grid (Kubota et al.
135 2007; Aonashi et al. 2009).

136 Fractional cloudiness and radiation data are obtained from the Clouds and the Earth's Radiant
137 Energy System (CERES) product at 3-hourly intervals on a 1° grid (Wielicki et al. 1996) and the
138 Pacific Northwest National Laboratory (PNNL) Combined Retrieval (CombRet) product based on
139 cloud and thermodynamic profile measurements at Gan Island (Feng et al. 2014). The CombRet
140 product is only available from 10 October onward.

141 ECMWF OA at 0.25° horizontal resolution, 18 vertical levels from the surface to 50 hPa, and
142 six-hourly intervals are used to help constrain and extend the sounding-based analyses beyond the

143 NSA and SSA domains. Unlike TOGA COARE, soundings outside the core DYNAMO area were
144 extremely sparse, so such a procedure is needed to supplement the soundings. Furthermore, the
145 ECMWF analyses were utilized to replace sounding data from ships when they were off station
146 since the quality of the analyses is degraded when the network collapses from a quadrilateral
147 to a triangle (Katsumata et al. 2011). Procedures for incorporating ECMWF OA in a way that
148 enhances the analysis but minimally impacts derived fields such as divergence are described in the
149 next subsection.

150 Surface fluxes and SST fields over the Indian Ocean are from the TropFlux product (daily values,
151 1° horizontal grid) based on Kumar et al. (2012). To check the reliability of the TropFlux data for
152 DYNAMO, surface fluxes and SST from that product are compared to in situ measurements from
153 the R/V *Revelle*, made available via <ftp://dynamo.dms.uconn.edu/> through a collaborative effort
154 between NOAA/Physical Sciences Division/ESRL, Oregon State University, and the University of
155 Connecticut.

156 *c. Data analysis procedures*

157 While the sounding sites comprising the SSA conducted 8-per-day launches (Fig. 1), the two
158 northern sites – Malé and Colombo – had a nominal launch frequency of 4 per day. Since there
159 is a considerable interest in the diurnal cycle over both arrays (to be reported on in a compan-
160 ion paper, Ruppert and Johnson (2014), submitted to the *J. Atmos. Sci.*), the 6-hourly Malé and
161 Colombo sounding data have been linearly interpolated in time to allow for budgets to be carried
162 out at 3-hourly intervals over both the NSA and SSA. Interpolated soundings were only created if
163 the time gap between soundings was less than or equal to the nominal 6-hourly sounding interval.
164 The interpolation procedure was also used to fill in a handful of 6-h gaps in sounding data for the
165 SSA. An evaluation of the impact of this procedure at Gan Island where 3-hourly soundings were

166 taken throughout the experiment shows that the interpolation procedure results in relatively small
167 errors. Specifically, rms differences in temperature, specific humidity, and winds between contem-
168 poraneous interpolated and actual soundings are ~ 0.5 C, 0.5 g kg $^{-1}$, and 1 m s $^{-1}$, respectively.

169 Owing to the large data-void regions outside the core sounding arrays, the ECMWF OA was used
170 at 5° grid intersections if no observations (soundings, satellite winds or otherwise) were present
171 within a 4.5° radius of such an intersection. To facilitate its use at 3-h intervals, the ECMWF
172 OA was linearly interpolated in time to create a 3-h resolution product. *Since this procedure to*
173 *enhance data coverage was only applied outside the main core arrays, results in the interior are*
174 *largely independent of model analyses and hence parameterizations of physical processes*, as will
175 be quantitatively demonstrated in Section 6a. One exception is when ships were offsite, in which
176 case model analyses filled in for missing ship soundings. Only during these periods did the model
177 analyses noticeably impact budget quantities over the arrays. In recognition of the fact that the
178 results have model influence during these periods, port-call intervals are specifically denoted in
179 time series plots by shading or other designations.

180 Following interpolation to 3-hourly intervals, the sounding data, along with the other observa-
181 tions and model fields described above, were objectively analyzed onto a 1° by 1° grid at the sur-
182 face and at 25-hPa intervals from 1000 to 50 hPa over the entire domain shown in Fig. 1 using the
183 multiquadric interpolation procedure as described in Ciesielski et al. (1997). Quality-controlled
184 sounding data from sites shown in Fig. 1 outside the arrays were used to help constrain the anal-
185 yses. Corrections to the divergence were made such that vertical motion balanced to zero at the
186 tropopause level (typically at 100 hPa), which was determined at each grid point and time step
187 (Johnson and Ciesielski 2002).

188 3. Budget analysis considerations

189 Following Yanai et al. (1973), but including ice processes, we write the equations for the appar-
 190 ent heat source and moisture sink as follows:

$$\begin{aligned}
 Q_1 &\equiv \frac{\partial \bar{s}}{\partial t} + \bar{\mathbf{v}} \cdot \nabla \bar{s} + \bar{\omega} \frac{\partial \bar{s}}{\partial p} \\
 &= L_v(\bar{c} - \bar{e}) + (L_v + L_f)(\bar{d} - \bar{s}_*) + L_f(\bar{f} - \bar{m}) + Q_R - \frac{\partial}{\partial p}(\overline{s'\omega'}), \quad (1)
 \end{aligned}$$

$$\begin{aligned}
 Q_2 &\equiv -L_v \left[\frac{\partial \bar{q}}{\partial t} + \bar{\mathbf{v}} \cdot \nabla \bar{q} + \bar{\omega} \frac{\partial \bar{q}}{\partial p} \right] \\
 &= L_v(\bar{c} - \bar{e}) + L_v(\bar{d} - \bar{s}_*) + L_v \frac{\partial}{\partial p}(\overline{q'\omega'}), \quad (2)
 \end{aligned}$$

191 where c , e , d , s_* , f , and m are condensation, evaporation, deposition, sublimation, freezing, and
 192 melting rates; q is the water vapor mixing ratio; $s \equiv c_p T + gz$ the dry static energy; Q_1 the apparent
 193 heat source; Q_2 the apparent moisture sink; Q_R the net radiative heating rate; L_v and L_f the latent
 194 heats of vaporization and fusion; overbar refers to a horizontal average; primes a deviation from
 195 this average; and horizontal eddy flux divergences are assumed to be small.¹

196 Integration of (1) and (2) from the tropopause pressure p_T to surface pressure p_0 yields

$$\langle Q_1 \rangle = \langle Q_R \rangle + L_v P_0 + \langle L_f(\bar{d} - \bar{s}_*) \rangle + \langle L_f(\bar{f} - \bar{m}) \rangle + S_0 \quad (3)$$

$$\langle Q_2 \rangle = L_v(P_0 - E_0), \quad (4)$$

¹A more accurate representation of the moist thermodynamics includes conservation equations for vapor and airborne condensate, precipitation mass, and the entropy of moist air (e.g., Ooyama 1990). However, owing to the lack of direct measurements of microphysical processes and precipitation rates over the sounding arrays, we use the formulation of Yanai et al. (1973).

197 where $\langle \quad \rangle \equiv 1/g \int_{p_T}^{P_0} (\quad) dp$, the surface precipitation rate is $P_0 = \langle \bar{c} - \bar{e} + \bar{d} - \bar{s}_* \rangle$, S_0 is the
 198 surface sensible heat flux, and E_0 the surface evaporation rate. In the following analysis, it is
 199 assumed that over the large sounding arrays and long time scales considered the terms $\langle L_f(\bar{d} -$
 200 $\bar{s}_*) \rangle$ and $\langle L_f(\bar{f} - \bar{m}) \rangle$ in (3), for which there are no direct measurements, are comparatively
 201 small. Therefore, we make the following approximation, as in Yanai and Johnson (1993):

$$\langle Q_1 \rangle \cong \langle Q_R \rangle + L_v P_0 + S_0 . \quad (5)$$

202 As a check on this assumption, the Goddard Cumulus Ensemble modeling results of Tao et al.
 203 (2003) applied to the convectively active periods of the South China Sea Monsoon Experiment
 204 (SCSMEX) give a ratio of $\langle L_f(\bar{d} - \bar{s}_*) \rangle$ to $L_v P_0$ in (3) of ~ 0.03 , while the ratio of $\langle L_f(\bar{f} - \bar{m}) \rangle$
 205 to $L_v P_0$ is far smaller.

206 Locally, however, e.g., averaged separately over the convective and stratiform regions of a trop-
 207 ical squall line, the above omitted terms are not negligible. These terms could also be important
 208 when there is a substantial build-up or decay in precipitation systems, even over large areas. For
 209 example, as convection builds up within the NSA during the developing phase of the MJO, there
 210 could be considerably more deposition than sublimation, as well as more freezing than melting,
 211 during a time interval of days, with the opposite being true during a decay phase. The latter sit-
 212 uation is related to hydrometeor storage, which can be important on diurnal time scales (McNab
 213 and Betts 1978) or when the cloud volume is changing rapidly and/or when there is an advection
 214 of hydrometeors into or out of a region. An attempt was made by Johnson (1980) to estimate
 215 hydrometeor storage effects for a composite easterly wave during the GARP Atlantic Tropical Ex-
 216 periment, but determination of the evolving cloud and precipitation fields posed serious challenges
 217 and the computations contained considerable uncertainty. While we have future plans to utilize
 218 satellite, radar, and other data to investigate such storage effects, they are excluded from this study.

219 Defining moist static energy as $h \equiv s + L_v q$, subtraction of (2) from (1) and integration from
 220 the tropopause to any level p (neglecting the terms involving L_f) yields an expression for F , the
 221 vertical eddy flux of h :

$$F(p) \equiv -\frac{1}{g} \overline{(h' \omega')_p} \cong \frac{1}{g} \int_{p_T}^p (Q_1 - Q_2 - Q_R) dp, \quad (6)$$

222 or upon integration to the surface, we have following Yanai et al. (1973):

$$F_0 \equiv F(p_0) = S_0 + L_v E_0 \cong \langle Q_1 \rangle - \langle Q_2 \rangle - \langle Q_R \rangle. \quad (7)$$

223 An alternate version of (7) can be written as

$$\langle \frac{\partial \bar{h}}{\partial t} \rangle + \langle \bar{\mathbf{v}} \cdot \nabla \bar{h} \rangle + \langle \bar{\omega} \frac{\partial \bar{h}}{\partial p} \rangle = \langle Q_1 \rangle - \langle Q_2 \rangle \cong S_0 + L_v E_0 + \langle Q_R \rangle. \quad (8)$$

224 Sobel et al. (2014) used (8) along with the sounding data employed in this study and also ERA
 225 Interim reanalysis data to investigate the moist static energy budget for the October and November
 226 MJOs. That analysis will not be repeated here, but we will relate our findings to theirs where
 227 appropriate.

228 The above set of equations can be used to check the accuracy of the budgets. The surface
 229 precipitation rate P_0 can be estimated from the moisture or heat equations, (4) or (5), but since \langle
 230 $Q_R \rangle$ is not directly measured, and (5) is an approximation, we use (4), with E_0 from TropFlux, to
 231 compute P_0 and compare those values with independent satellite-based estimates for the sounding
 232 arrays.

233 We use (7) to compute $\langle Q_R \rangle$, again using surface fluxes from TropFlux, and compare these
 234 values with independent estimates from CERES (for the arrays) and PNNL (for Gan Island). Fol-
 235 lowing the procedures in Johnson and Ciesielski (2000), we also include several additional effects,

236 which act in the direction to increase, albeit slightly, the diagnosed radiative cooling rate. They are
237 (1) the effects of mass sources and sinks resulting from precipitation and surface evaporation on
238 the computation of vertical motion (Trenberth 1991); (2) the sensible heat flux due to rain, which
239 falls at the wet-bulb temperature (Gosnell et al. 1995); and (3) frictional dissipation associated
240 with falling precipitation (Emanuel and Bister 1996).

241 In past budget studies, we did not have sufficient information on the vertical structure of Q_R to
242 compute the vertical profile of F . For DYNAMO, however, we have the PNNL CombRet product
243 that provides the vertical profile of Q_R (Feng et al. 2014), so $F(p)$ can be computed. Unfortunately,
244 cloud measurements taken at the AMIE site on Gan Island undersampled high-level cirrus clouds
245 due to signal attenuation in heavy rainfall, so their effects are not fully represented in the CombRet
246 radiative heating rates. As a result, the CombRet net-tropospheric radiative cooling during the
247 cirrus-abundant convectively active phase of the MJO is somewhat overestimated compared to the
248 CERES product, as will be shown later. Therefore, for the computation of F , we adjust the profile
249 of Q_R from CombRet by a constant fraction at each level so that its vertical integral matches that
250 of the CERES product. Ideally, this adjustment should be distributed vertically in a realistic way,
251 but we do not have sufficient information to do so at this time.²

252 **4. Broad-scale distributions of rainfall**

253 *a. Surface flux estimates used in rainfall computations*

254 Computations of precipitation and radiative heating rates over the arrays rely on estimates of
255 surface fluxes over the enclosed areas. Two flux products have been tested: the Woods Hole

²In addition to the cirrus cloud issue, it has been pointed out to the authors by Adam Sobel that the lower boundary for the surface longwave flux in CombRet was taken to be land, which is unrepresentative of the surrounding ocean and differs from the corresponding CERES value by several tens of W m^{-2} .

256 Oceanographic Institution (WHOI) Objectively Analyzed air-sea Fluxes (OAFlux) based on Yu
257 and Weller (2007) and TropFlux (Kumar et al. 2012). Similar results were obtained for both
258 products; however, since TropFlux yields slightly better agreement with the latent heat flux with
259 measurements at the *Revelle* and slightly better correlations of computed rainfall rates to those
260 observed, we employ that product for the following analyses.

261 To evaluate the accuracy of TropFlux for DYNAMO, surface fluxes from that product are com-
262 pared to bulk fluxes at the R/V *Revelle* computed using the COARE 3.0 algorithm (Fairall et al.
263 1996). The mean of TropFlux values that fall within a 1° radius of *Revelle*'s nominal position are
264 plotted in Fig. 2 along with daily-averaged *Revelle* fluxes when the ship is on station. SST from
265 the *Revelle* are also shown in Fig. 2, as is the mean TRMM rainfall within the 1° radius of the
266 site. The surface sensible and latent heat fluxes and SST, both the daily and SOP-mean values,
267 show generally good agreement throughout much of the period, although there are occasions of
268 disagreement (e.g., the SST in mid-November). Part of the disagreement is likely related to the
269 fact that one data source (*Revelle*) is a point measurement and the other (TropFlux) is an area
270 measurement. SOP-mean values of S_0 , $L_v E_0$, and SST are $10\text{-}11 \text{ W m}^{-2}$, $106\text{-}107 \text{ W m}^{-2}$, and
271 29.5°C , respectively. These values are in close agreement with the those reported over the western
272 Pacific during TOGA COARE (Weller and Anderson 1996).

273 *b. Large-scale temporal and spatial distributions of rainfall*

274 Using surface latent heat fluxes over the Indian Ocean from TropFlux, 3-day running mean
275 filtered daily-average rainfall rates computed from (4) are compared to TRMM 3B42 estimates (3-
276 hourly, unfiltered) in Fig. 3. In the longitude band of the sounding arrays ($72\text{-}80^\circ\text{E}$), the analysis is
277 based on the sounding data whereas outside the arrays, it is based principally on the ECMWF OA.
278 Though peak amplitudes in the moisture budget rainfall are reduced by the filtering, the spatial

279 and temporal distribution of budget estimates agree well with the TRMM envelopes of convection
280 for the two MJO events in October and November. This filtered version of the budget analysis
281 does not capture the higher-frequency disturbances embedded within the MJOs (Gottschalck et al.
282 2013), such as the two-day disturbances within the active phase of the MJO in October (Zuluaga
283 and Houze 2013; Johnson and Ciesielski 2013). Analyses of the heat and moisture budgets for
284 these disturbances is left for future work.

285 A broad-scale depiction of the SOP-mean rainfall rate over the Indian Ocean for October and
286 November is presented in Fig. 4. Rainfall rate diagnosed from the moisture budget is in overall
287 good agreement with the TRMM estimates both in terms of magnitude and areal distribution.
288 A prominent feature of the rainfall pattern is an ITCZ-like band between the equator and 10°S
289 extending across much of the Indian Ocean. Slightly greater SOP-mean rainfall rates can be seen
290 over the SSA than the NSA in both TRMM (9.1 vs. 8.9 mm day⁻¹) and the budgets (10.6 vs. 9.4
291 mm day⁻¹).

292 **5. Heat and moisture budgets for sounding arrays**

293 *a. Time series for Special Observing Period (SOP)*

294 Time series of the apparent heat source Q_1 and apparent moisture sink Q_2 over the NSA for
295 October and November are shown in Fig. 5, along with NSA daily-mean rainfall from TRMM.
296 The MJO heavy-rain periods in the latter half of both months are accompanied by pronounced
297 increases in the amplitudes of Q_1 and Q_2 . It should be noted that as expected, the rainfall time
298 series for the entire NSA shown in Fig. 5 does not correlate well with that for a single location,
299 namely, at the *Revelle* (Fig. 2), but it does represent well the convectively active periods of the
300 October and November MJOs (Fig. 3).

301 The evolution of Q_1 and Q_2 through both MJO events (Fig. 5) shows a similar progression to
302 that observed during TOGA COARE (Lin and Johnson 1996): shallow, non-precipitating cumu-
303 lus indicating lower-tropospheric moistening (negative Q_2) during the suppressed periods (RMM
304 phases 6-8 and the early portion of 1), followed by cumulus congestus (low-to-midlevel peaks
305 in Q_1 and Q_2 in RMM phase 1 and early part of 2), then deep convection (higher peaks in Q_1
306 and Q_2 in RMM phases 2 and 3), and finally stratiform-like profiles of Q_1 and Q_2 (positive val-
307 ues aloft, negative at low levels in RMM phases 3 and 4). This progression is consistent with
308 now generally accepted paradigm for the evolution of precipitation systems and diabatic heating
309 through the life cycle of the MJO (Johnson et al. 1999; Kiladis et al. 2005; Zhang 2005; Mapes
310 et al. 2006; Benedict and Randall 2007; Haertel et al. 2008). A notable difference between the
311 two events, however, is the longer duration of both the build-up and convectively active periods
312 for the October MJO compared to the November MJO. In addition, the convective moistening by
313 shallow cumulus during the suppressed periods was stronger for the October than the November
314 event. It is also noted that the maxima in heating and drying in Fig. 5 are coincident with peaks in
315 NSA-averaged TRMM rainfall, both in connection with the two-day disturbances in late October
316 (Zuluaga and Houze 2013) and the two Kelvin waves in November. This correspondence between
317 the Q_1 and Q_2 peaks and rainfall lends confidence to the budget results for DYNAMO.

318 There has been evidence from past studies of a stepwise progression of the cloud fields from
319 shallow cumulus to congestus to deep convection (Kikuchi and Takayabu 2004; Yoneyama et al.
320 2008; Virts and Wallace 2010; Del Genio et al. 2012), as well as in preliminary results from DY-
321 NAMO itself in high-resolution time series of relative humidity at Malé, Gan Island, and the R/V
322 *Revelle* (Fig. 13 of Johnson and Ciesielski 2013). The results in Fig. 5 are suggestive of a similar
323 behavior; namely, there are approximately 5-day periods (15-20 October and 17-22 November) of
324 low-to-midtroposphere heating and drying conceivably associated with cumulus congestus popu-

325 lations. This relationship will be further explored in terms of the eddy fluxes of moist static energy
326 F later in Section 8. However, definitive conclusions regarding stepwise evolution of cloud pop-
327 ulations will have to await further work integrating sounding budget findings with research radar
328 observations, which is beyond the scope of the present study.

329 The time series of Q_1 and Q_2 over the SSA (Fig. 6) contrasts markedly to that over the NSA
330 even though both arrays share the common sites Gan Island and *Revelle*. As noted in Johnson and
331 Ciesielski (2013), the MJO signal during the October-November period of DYNAMO was stronger
332 north of the equator during this boreal fall period. Frequent episodes of rainfall corresponding to
333 periods of heating/drying occurred throughout the two-month period with a moderate increase in
334 convective activity associated with the MJOs toward the ends of October and November. As can
335 be seen from Fig. 4, the SSA straddled an ITCZ-like band of precipitation between the equator
336 and 10°S , which is reflected in the semi-permanent precipitation in that array.

337 *b. Mean profiles for SOP*

338 SOP-mean vertical profiles of Q_1 and Q_2 for the NSA and SSA, along with frequency-altitude
339 diagrams for each, are shown in Fig. 7. The amplitudes of the profiles are similar between the
340 two arrays, consistent with the approximate agreement in TRMM 3B42-estimated rainfall for the
341 NSA (8.9 mm day^{-1}) and SSA (9.1 mm day^{-1}). The Q_1 and Q_2 profile shapes are similar over the
342 NSA, while the peaks are widely separated over the SSA. These results suggest a greater fraction
343 of stratiform precipitation over the NSA than the SSA (e.g., Luo and Yanai 1984). This inference
344 is supported by the frequency-altitude diagrams for the NSA (Fig. 7), which show a greater spread
345 of negative Q_2 values (indicative of moistening by evaporation) and a higher frequency of negative
346 Q_1 values (cooling) in the lower troposphere (between 900 and 600 hPa) than for the SSA.

347 Three research radars were deployed in DYNAMO, but their precipitation area coverage is a
348 small fraction ($\sim 8\text{-}9\%$) of the areas of the sounding arrays, so they cannot be used to check the
349 inference of greater stratiform rain fraction over the NSA. Analysis of the convective/stratiform
350 fractions from the TRMM 2A25 product does show a greater stratiform fraction for the NSA
351 (55%) than the SSA (50%), although the sampling for the two-month period is limited. In partic-
352 ular, there were 102 (117) TRMM overpasses for the NSA (SSA) during the SOP; nevertheless,
353 the 5% difference is significant at the 95% level using a one-sided student t-test. These TRMM
354 stratiform fractions are greater than the tropical global estimate of $\sim 40\%$.³ although the TRMM
355 climatologies of Schumacher and Houze (2003) and Funk et al. (2013) show higher values (by
356 about 5%) over the central Indian Ocean. Recent analyses of the SMART-R radar data on Gan Is-
357 land by DePasquale et al. (2014) indicate a mean stratiform rain fraction of 41% for what they refer
358 to as the active periods of the October, November, and December MJOs. Despite the disagreement
359 in magnitudes, the TRMM estimates for DYNAMO do show a greater stratiform contribution to
360 rainfall over the NSA than the SSA, which is consistent with the budget findings. Considering
361 that the MJO signal was stronger over the NSA than the SSA (Johnson and Ciesielski 2013), these
362 findings are also consistent with the results of Lin et al. (2004) that indicate a greater stratiform
363 rain fraction within the MJO convective envelope than the tropical mean.

³This estimate was recently revised downward to $\sim 35\%$ by Funk et al. (2013) based on a consideration of misclassification of some shallow clouds as stratiform in the TRMM 2A23v7 algorithm. Similar downward adjustments are likely needed for the DYNAMO estimates for the NSA and SSA.

364 **6. Precipitation rate intercomparisons**

365 *a. Impact of ECMWF operational analysis data on budgets*

366 As noted earlier, the ECMWF OA has been used outside the sounding arrays, but also in proxim-
367 ity to the R/V *Revelle* and *Mirai* when those ships were off station in order to improve the analyses
368 during the port-call periods. To demonstrate this improvement, and to also show the minor effects
369 of the model analyses at other times, a time series of rainfall rate computed from the Q_2 budget
370 for the NSA with and without ECMWF analyses is shown in Fig. 8 (upper panel). Outside the
371 port-call period, there is mostly only a minor change in the rainfall estimates by the inclusion of
372 ECMWF OA (Fig. 8, lower panel), supporting the assertion of minimal impact of model analy-
373 ses when all sites were occupied. A similar comparison of the divergence profiles (not shown)
374 indicates little impact by the model analyses during that period. Overall, the budget and TRMM
375 rainfall rates agree well, and the agreement during the port-call period improves with the inclusion
376 of ECMWF OA (values are generally overestimated without ECMWF OA). Averaged over the en-
377 tire SOP, the addition of ECMWF OA brings the NSA mean budget rainfall rate (9.4 mm day^{-1})
378 more in line with the TRMM estimate (8.9 mm day^{-1}). The budget estimate for the NSA area and
379 for the two-month period corresponding to the SOP is subject to a random sampling error of 0.3
380 mm day^{-1} based on the work of Mapes et al. (2003).

381 *b. Intercomparison of budget and satellite estimates*

382 A comparison between the budget rainfall estimates and those for four different satellite products
383 is shown in Fig. 9 and Table 1 for both the NSA and SSA. There is good agreement among the
384 various satellite products and the budgets for the NSA: satellite estimates ranging from 8.9 to
385 9.8 mm day^{-1} compared to the budget 9.4 mm day^{-1} . The agreement is slightly poorer for the

386 SSA: 8.2 to 9.7 mm day⁻¹ compared to the budget 10.6 mm day⁻¹. For the NSA, temporal
387 correlations between budget estimates and TRMM, CMORPH, GPCP, and GSMaP (all with 3-
388 day running-mean filtering of daily-average values) are 0.97, 0.96, 0.93, and 0.93, respectively.
389 The correlations for the SSA are not quite as good: 0.92, 0.90, 0.82, and 0.86, respectively, for
390 the same products; nevertheless, the correlations for both the NSA and SSA are significant at the
391 99% level using a one-sided student t-test. For both the NSA and the SSA, the budget estimates
392 exceed the satellite estimates during much of the suppressed phases (most of RMM phases 8 and
393 1, as well as 7 in November) while the opposite is true during the MJO convectively active phases
394 (much of RMM phases 2 and 3). Using shipborne radar data from the *Revelle*, Xu and Rutledge
395 (2014) show that the TRMM 3B42 product, which is based on a combination of microwave and
396 infrared data, underestimates rainfall during suppressed periods, presumably owing to insufficient
397 sampling of shallow, warm-rain cells, while it overestimates rainfall during the convectively active
398 phases, likely due to the abundance of high-level cloudiness at those times. These deficiencies in
399 the satellite products are in the right direction to explain at least some of the differences between
400 the budgets and satellites in Fig. 9. The fact that there is a greater discrepancy for the SSA (budgets
401 exceeding the satellite estimates) may be related to the more frequent occurrence in the SSA of
402 light-to-moderate rain episodes, when satellites tend to underestimate rainfall, and weaker, briefer
403 heavy rain episodes associated with the MJOs, when the high-level cloud coverage and stratiform
404 rain fractions are higher (Barnes and Houze 2013; Powell and Houze 2013; DePasquale et al.
405 2014) and satellites tend to overestimate rainfall (Liu et al. 2007; Xu and Rutledge 2014).

406 The mean NSA budget rainfall rate for the DYNAMO SOP (9.4 mm day⁻¹) is comparable to the
407 mean value of 8.4 mm day⁻¹ for the four-month Intensive Observing Period (IOP) of the TOGA
408 COARE Intensive Flux Array (IFA) (Table 1). The correlations between the budget and satellite-
409 based rainfall estimates for DYNAMO, all exceeding 0.90 for the NSA, represent an improvement

410 over the TOGA COARE IFA budget and satellite rainfall rate correlations that were closer to 0.80
411 (Ciesielski et al. 2003).

412 Also seen in Fig. 9 are the possible effects of hydrometeor storage on the budgets (McNab and
413 Betts 1978; Johnson 1980), particularly over the NSA for the October MJO. During the period
414 of increasing precipitation between October 15 and 22, the budget rainfall rate exceeds all of the
415 satellite estimates, but the reverse is true toward the end of October. The discrepancy for the 15-22
416 October period may be related to the storage of water in clouds as the cloud area increased rapidly
417 (as shown in the next section), whereas the reverse situation at the end of the month is presumably
418 a result of evaporation of cloud systems generated at an earlier time as the cloud area decreased
419 rapidly. Evidence of storage effects is not as obvious for the November MJO. Determination of
420 cloud storage effects is complicated, requiring estimates of changing cloud volumes within the
421 arrays, cloud water mixing ratios, etc., and is beyond the scope of the present study.

422 **7. Intercomparison of radiative heating rates**

423 *a. Budget-satellite intercomparisons, relationship to cloud cover*

424 In this section we compare $\langle Q_R \rangle$ obtained from the combined heat and moisture budgets
425 and surface fluxes (7) with the CERES and PNNL radiation products. However, we first show a
426 time series of the vertical profile of daily-averaged Q_R from the PNNL CombRet product for Gan
427 Island (Feng et al. 2014), along with three-month mean values of shortwave, longwave, and net
428 radiative heating (Fig. 10). The October and November MJOs are clearly seen to modulate Q_R , as
429 does another MJO-like event in December described by Gottschalck et al. (2013) and Yoneyama
430 et al. (2013). During the convectively active phases in the latter halves of the months, greatly
431 reduced net radiative cooling, even reverting to a net heating at times, is seen to occur in the

432 midtroposphere (800 to 400 hPa) in response to the increased upper-level cloud cover (shown
433 later). In the upper troposphere between 400 and 200 hPa, intermittent enhanced cooling can be
434 seen, reflecting increased longwave cooling atop upper-level cloud systems. However, the overall
435 cooling in this layer is likely overestimated due to the undersampling of cirrus clouds by the
436 instrumentation on Gan Island (Feng et al. 2014). This conclusion is supported by the study of
437 Jiang et al. (2011), which shows a similar modulation of Q_R by the MJO from the TRMM-based
438 radiation algorithm of L'Ecuyer and McGarragh (2010), but the maximum heating (i.e., minimum
439 cooling) during the convectively active phases is shifted upward to near 300 hPa as opposed to the
440 peaks being centered more in the midtroposphere in the CombRet product. The weak heating near
441 100 hPa is attributable to localized heating in the $15 \mu\text{m CO}_2$ band owing to the sharp curvature in
442 the temperature profile (Thuburn and Craig 2002). The mean profile of Q_R shows a $\sim 1 \text{ K day}^{-1}$
443 net cooling averaged through the troposphere, with slightly greater cooling near the surface and in
444 the upper troposphere.

445 SOP time series of $\langle Q_R \rangle$ from the budgets and other independent estimates for the NSA and
446 SSA, along with SOP-mean values, are shown in Fig. 11 and Table 1. The budget and CERES
447 results are for the array areas, while the CombRet estimate is for the Gan Island location only.
448 Two curves are shown for the budget results, one with the inclusion of the effects of precipita-
449 tion/evaporation on the computation of divergence, sensible heat flux due to rain, and frictional
450 dissipation associated with precipitation (solid black curve) and one without (dashed black curve).
451 These effects are minor, but they bring the period-mean $\langle Q_R \rangle$ values, -0.59 and -0.53 K
452 day^{-1} , into closer agreement with the CERES SOP-mean values, -0.63 and -0.62 K day^{-1} , for
453 the NSA and SSA, respectively (Table 1). The CERES SOP-mean $\langle Q_R \rangle$ for the Gan Island
454 location is -0.60 K day^{-1} , very close to the NSA and SSA mean values. For the array areas and
455 two-month period of the SOP, the random sampling error for $\langle Q_R \rangle$ associated with the budget

456 results is 0.03 K day^{-1} (Mapes et al. 2003). In addition to the SOP-mean values, the temporal
457 variability of the budget and CERES $\langle Q_R \rangle$ are in reasonable agreement, although there are
458 certain periods (first half of October and late November) where the disagreement is large. The
459 differences during these periods are not fully understood, although part of the explanation likely
460 lies in the fact that the computation of $\langle Q_R \rangle$ from (8) involves a small difference between two
461 large quantities ($\langle Q_1 \rangle$ and $\langle Q_2 \rangle$) and hence is also quite sensitive to S_0 and $L_\nu E_0$.

462 The budget-mean value of $\langle Q_R \rangle$ for the DYNAMO arrays is very close to the value of -0.55
463 K day^{-1} obtained for the TOGA COARE IFA by Ciesielski et al. (2003) using the same budget
464 methodology (Table 1). In addition, the large-amplitude variation of $\langle Q_R \rangle$ over the life cy-
465 cles of the DYNAMO MJOs closely resembles that observed for the major December 1992 MJO
466 event in TOGA COARE (Johnson and Ciesielski 2000). Past studies have shown that this hor-
467 izontal variability can have substantial impacts on the tropical Walker and Hadley circulations
468 (Hartmann et al. 1984; Slingo and Slingo 1988, 1991; Randall et al. 1989; Sherwood et al. 1994;
469 Webster 1994; Raymond 2000). In addition, the reduction in radiative cooling (increase in column-
470 integrated radiative heating) beginning in the middle of October and November as cirrus started
471 to increase [also observed for the December MJO during TOGA COARE (Johnson and Ciesielski
472 2000)] could play an important role in the build-up of moist static energy prior to the active phases
473 of the MJOs (Chikira 2014; Sobel et al. 2014). Qualitatively, the modulation of $\langle Q_R \rangle$ by the
474 MJOs is similar in the CombRet estimate, though the SOP-mean net cooling rate (-0.81 K day^{-1})
475 is greater. This discrepancy is likely related in part to the undersampling of upper-tropospheric
476 clouds by the instrumentation on Gan Island, and hence exclusion of their full effects in the radia-
477 tion calculations.

478 The time series of budget and CERES $\langle Q_R \rangle$ for the NSA are repeated in Fig. 12 (middle
479 panel), but to better illustrate the full cycle of the November MJO, for a slightly longer period

480 than the SOP (until December 6 when six-hourly soundings on Colombo were terminated). Also
481 included are a time series of relative humidity (upper panel) and cloud fractional area from the
482 CERES product for low, low-middle, high-middle and high clouds (lower panel). Figure 12
483 shows a strong correlation of the net tropospheric radiative heating with upper-tropospheric clouds,
484 namely, $|\langle Q_R \rangle|$ decreases (increases) as the high clouds increase (decrease). This result con-
485 firms the important role of high-level clouds in trapping longwave radiation in the troposphere
486 (e.g., Hartmann et al. 1992; Stephens et al. 1994). The fractional area of shallow clouds is seen to
487 decrease during the convectively active phases of the MJO (Zuluaga and Houze 2013); however,
488 there may be some blocking of the satellite detection of shallow clouds by upper-level cloud layers.
489 There is a slight increase in middle-low cloud coverage in the middle of October and November,
490 consistent with the implied increase in congestus activity during those times from the heat and
491 moisture budgets (Fig. 5). Detailed comparisons of the budget results with cloud populations
492 measured by the DYNAMO research radars is left for future study.

493 Also evident from Fig. 12 is an increase in upper-tropospheric relative humidity in the middle of
494 each month, consistent with the increase in high-level clouds and a corresponding reduction in $|\langle$
495 $Q_R \rangle|$ that occurred at those times. As noted in (Johnson and Ciesielski 2013, their Fig. 11), this
496 moistening was associated with a cool anomaly aloft (between 200 and 100 hPa) in mid-October
497 in advance of the convectively active phase of the MJO. The tilted warm-cool anomaly pattern
498 that was observed during DYNAMO (Johnson and Ciesielski 2013) resembled that first described
499 by Kiladis et al. (2001), who explained this feature as a gravity wave response to the large-scale
500 MJO convective heat source envelope. It is consistent with the recent findings of Virts and Wallace
501 (2010) and Virts et al. (2010), who determined from an analysis of CALIPSO cirrus data that the
502 coldest, cloudiest anomalies aloft occur $\sim 30^\circ$ east of the main MJO convective heat source and

503 descend with time, which is qualitatively consistent with the moisture anomalies observed during
504 DYNAMO (Fig. 12).

505 *b. Assessment of radiative-convective instability*

506 The possible role of radiative forcing in the dynamics of the MJO can be assessed by compar-
507 ing column-integrated values of radiative to convective heating. Using a full-physics GCM, Lee
508 et al. (2001) argued that if this ratio exceeds approximately 20%, then the atmosphere can reach
509 radiative-convective instability (Yu et al. 1998; Raymond 2001). However, whether such an in-
510 stability exists has been proposed to be further dependent on the normalized gross moist stability
511 (NGMS: Neelin and Held 1997; Raymond et al. 2009; Sobel and Maloney 2012). Sobel and Mal-
512 oney (2013) posit that if the column-integrated radiative to convective heating ratio is greater than
513 NGMS, then an instability can exist. Physically, this means that radiative heating increases the
514 moist static energy in the column faster than the vertical motion and associated circulation can
515 export it.

516 In Fig. 13, a comparison is shown between the anomalies (based on SOP-means, seasonal trends
517 not removed) of column-integrated convective heating $L_v P_0 + S_0 \equiv \langle Q_{conv} \rangle$ from the budgets and
518 flux data and $\langle Q_R \rangle$ from the CERES product for DYNAMO (upper panel), the ratio of cloud
519 radiative forcing $\langle Q_R \rangle_{CF}$ to $\langle Q_{conv} \rangle$ (middle panel), and a time series of TRMM precipitation
520 for the SOP (lower panel). Past work by Lin and Mapes (2004) using various budget and radia-
521 tion data sets showed that for the December 1992 TOGA COARE MJO, the column-integrated
522 radiative heating lagged the column-integrated convective heating by about five days and the en-
523 hancement to the convective heating was about 10-15%. This enhancement fell short of the $\sim 20\%$
524 Lee et al. (2001) estimate as necessary for the atmosphere to reach radiative-convective instability
525 (Yu et al. 1998; Raymond 2001). Lin and Mapes (2004) speculated that the enhancement factor

526 might be larger, exceeding 20%, over the Indian Ocean and the recent study of Jiang et al. (2011)
527 using satellite and reanalysis data seems to bear this out.

528 However, Sobel and Maloney (2012, 2013) hypothesize that the existence of radiative-convective
529 instability is dependent not just on the enhancement factor, but also its size in relation to NGMS.
530 For DYNAMO, the time series of the column-integrated radiative/convective heating ratio (middle
531 panel) indicates an enhancement factor mostly between 10 and 20%, exceeding 20% occasionally.
532 These values are comparable to the total NGMS reported by Sobel et al. (2014) using both the
533 DYNAMO budget data set and ERA Interim, suggesting from Sobel and Maloney (2013) that
534 radiative-convective instability is indeed a possibility for the DYNAMO MJOs.

535 **8. Vertical flux of moist static energy**

536 The vertical eddy flux of h (or F), provides a measure of the activity of cumulus convection
537 (Yanai et al. 1973). Given the same rainfall rate in two different settings, if F in the midtropo-
538 sphere is large (small), the precipitation processes producing the rainfall are largely convective
539 (stratiform). The determination of $F(p)$ as a function of time in past field campaigns such as
540 TOGA COARE has been difficult owing to the lack of knowledge about vertical structure of the
541 net radiative heating rate, $Q_R(p)$, as a function of time. As noted earlier, we use the PNNL Com-
542 bRet Q_R product in the computation of F , but since the cooling is overestimated due to the lack of
543 high-cloud measurements on Gan Island, we adjust the CombRet $Q_R(p)$ by a constant factor such
544 that its vertical integral matches $\langle Q_R \rangle$ from array-averaged CERES values.⁴ In the computation
545 of $F(p)$, we integrate downward from the tropopause assuming the eddy fluxes are zero at that
546 level.

⁴CombRet data are not available for the period 1-9 October, so the vertical profiles for that period are approximated using CombRet $Q(p)$ for the period 12-17 November, which had a similar mean relative humidity profile. Both of these periods experienced suppressed conditions and were characterized with similar budget profiles and CERES $\langle Q_R \rangle$.

547 A time series of F for the NSA is shown in Fig. 14. Several levels of deep convective activity
548 are evident. First, in the light-rain periods from 1 to 15 October and 7 to 16 November, the eddy
549 fluxes are confined to the lower troposphere, consistent with the inference from Q_2 in Fig. 5 of
550 shallow, trade-like cumulus at those times. These periods are followed by \sim five-day periods of
551 eddy fluxes extending to the midtroposphere (15-20 October and 17-22 November), indicative of
552 cumulus congestus cloud populations (as also inferred from Fig. 5), and then later by \sim one-week
553 periods of strong eddy fluxes extending to the upper troposphere. Consistent with the profiles
554 of Q_1 and Q_2 in Fig. 5 and the time series of relative humidity at NSA sites (Fig. 13 of John-
555 son and Ciesielski 2013), a stepwise evolution of the cloud populations is suggested as opposed
556 to a smooth transition of the cloud fields. However, definitive conclusions on this matter can-
557 not be made from the budgets alone and work is currently underway to relate the budget results
558 to the cloud populations as determined by the research radars, similar to the studies of Powell
559 and Houze (2013) and (DePasquale et al. 2014). The deeper events in October were associated
560 with westward-moving, two-day disturbances (Zuluaga and Houze 2013; Johnson and Ciesielski
561 2013), while those in November were associated with Kelvin waves (Gottschalck et al. 2013; De-
562 Pasquale et al. 2014). The light-rain periods following the active periods of heaviest rainfall (1-4
563 and 29-30 November) were characterized by weak eddy fluxes, consistent with a prevalence of
564 stratiform precipitation. These results further support the accumulating evidence of a typical pat-
565 tern of shallow-to-congestus-to-deep-to-stratiform evolution of precipitation within the MJO, but
566 also indicate the shorter transition periods for the November than the October event.

567 The profiles of F for the SSA are strikingly different (Fig. 15). There are numerous instances of
568 strong eddy fluxes extending to the midtroposphere throughout the two-month period, consistent
569 with the results shown in Fig. 6. Although there are several strong events timed with the heavy
570 rainfall at the ends of October and November in connection with the MJOs, others occurred in

571 the suppressed phases of the events and are related to episodic disturbances within the ITCZ-like
572 precipitation band south of the equator.

573 SOP-mean NSA and SSA profiles of $Q_1 - Q_2 - Q_R$ and F , and SSA minus NSA differences in
574 those quantities are shown in Fig. 16. Once again, the substantially different mean characteristics
575 of convection in the two arrays are evident. The smaller separation of the Q_1 and Q_2 peaks in
576 the NSA leads to smaller values of $Q_1 - Q_2 - Q_R$ (i.e., the eddy flux convergence of moist static
577 energy) in the upper troposphere and weaker eddy fluxes F in the midtroposphere, consistent with
578 the higher stratiform fraction there as supported by the TRMM estimates. Comparison of F_0 from
579 the budgets with $S_0 + L_v E_0$ from TropFlux shown in Fig 16 indicate good agreement for the NSA
580 (128 vs. 115 W m^{-2} , respectively) but slightly poorer agreement for the SSA (138 vs. 116 W
581 m^{-2} , respectively).

582 **9. Summary and conclusions**

583 DYNAMO sounding data have been used to determine the apparent heat source Q_1 and appar-
584 ent moisture sink Q_2 for the northern and southern sounding arrays (NSA and SSA, respectively)
585 over the central Indian Ocean during the DYNAMO Special Observing Period (SOP; October-
586 November 2011). The sounding data have undergone extensive quality control prior to the compu-
587 tation of the budgets (Ciesielski et al. 2014a). In addition, a procedure has been applied to mitigate
588 the effects of the mountainous island of Sri Lanka on the Colombo soundings (Ciesielski et al.
589 2014b). Although ECMWF operational analyses have been used to describe the larger-scale char-
590 acteristics of the flow over the Indian Ocean during DYNAMO, the budget results for the sounding
591 arrays are largely model-independent. Surface precipitation rate P_0 from the moisture budget and
592 tropospheric net radiation $\langle Q_R \rangle$ from the combined budgets have been determined by incorpor-
593 ating surface sensible and latent heat flux measurements from TropFlux (Kumar et al. 2012). The

594 TropFlux measurements show good agreement with the in situ measurements of the bulk fluxes
595 at the R/V *Revelle*. The results for P_0 and $\langle Q_R \rangle$ are compared to independent satellite-based
596 estimates of these quantities. In addition, the availability of vertical profiles of radiative heating
597 rate from the AMIE facility on Gan Island has permitted computations of the vertical profile of
598 the vertical eddy flux of moist static energy. Finally, the budget results and CERES radiation
599 data are used to assess whether radiative-convective instability was operative for the MJOs during
600 DYNAMO.

601 Principal findings of the study are as follows:

- 602 • The spatial and temporal variation of the budget-derived rainfall rate over the Indian Ocean
603 during the SOP shows good agreement with the independent TRMM-based estimates. More-
604 over, the time series of array-averaged rainfall rate from the moisture budget agrees well with
605 the satellite-based estimates (TRMM, CMORPH, GPCP, and GSMAP).
- 606 • Prominent MJO signals were observed over the NSA, with a sequence of convective sys-
607 tem evolution inferred from Q_1 and Q_2 for both the October and November MJOs consistent
608 with numerous previous studies: shallow non-precipitating cumulus, followed by congestus
609 clouds, then deep convection, and finally stratiform precipitation. The two MJOs were oth-
610 erwise quite different. Stronger convective moistening by shallow cumulus was observed
611 leading up to the active phase in October than November. The duration of deep convective
612 activity was at least a week longer in the October MJO, and consisted of more short duration
613 (two-day) pulses in the heating than in the November MJO, the latter being dominated by two
614 prominent Kelvin-wave heating peaks.
- 615 • The time series of Q_1 and Q_2 for the SSA were strikingly different from the NSA, charac-
616 terized by frequent episodes of heating and drying in association with multiple precipitation

617 events. The MJO signal in the heating was still evident in the SSA, but smaller in amplitude
618 and principally manifest at the end of the events.

- 619 • The shapes of Q_1 and Q_2 vertical profiles were similar for the NSA, but less so for the SSA
620 where the peaks were widely separated, suggesting a greater stratiform rain fraction over the
621 NSA than the SSA. Though the sampling was limited, TRMM measurements support this
622 finding. The findings also support the work of Lin et al. (2004), which indicates that the
623 stratiform rain fraction for the MJO is greater than the tropical mean.
- 624 • The time series of $\langle Q_R \rangle$ from the budgets shows reasonable agreement with the satellite-
625 based CERES estimate, both indicating a significant modulation of $\langle Q_R \rangle$ by the MJO.
626 High-level clouds during the active phases of the both MJOs reduced the net-column radiative
627 cooling, even reverting $\langle Q_R \rangle$ to weak positive values at times, indicating the important role
628 of radiation in the moist static energy budget (Sobel et al. 2014). For the NSA, the budget
629 SOP-mean $\langle Q_R \rangle$ was -0.59 K day^{-1} compared to -0.63 K day^{-1} for CERES, while the
630 agreement was slightly poorer for the SSA (-0.53 vs. -0.62 K day^{-1} , respectively).
- 631 • Vertical profiles of the vertical flux of moist static energy for the NSA support the inferences
632 of the evolving cloud populations in the MJO based on the Q_1 and Q_2 results alone, namely, a
633 transition from shallow cumulus to congestus to deep convection and finally to stratiform pre-
634 cipitation. There is a suggestion of a stepwise evolution, supportive of past studies (Kikuchi
635 and Takayabu 2004; Yoneyama et al. 2008; Virts and Wallace 2010; Del Genio et al. 2012);
636 however, these findings are regarded as preliminary and require further study. The results for
637 the SSA are again strikingly different, indicating much more frequent episodes of convective
638 activity in the ITCZ, with an absence of the convective evolution seen for the NSA.

- 639 • The net-tropospheric radiative heating due to the cloud systems was approximately 20%, of
640 the same magnitude as the normalized gross moist stability (Sobel et al. 2014), suggesting a
641 possible role of radiative-convective instability (Yu et al. 1998; Raymond 2001) for the two
642 MJOs.

643 In addition to the budget analyses presented herein, large-scale forcing fields (e.g., Wu et al.
644 2000) have been computed and made available for application to cloud-resolving and single-
645 column models. The good agreement between budget integral constraints (i.e., rainfall, $\langle Q_R \rangle$,
646 surface fluxes) lends confidence to the accuracy of the forcing fields and their ability to capture the
647 large-scale signal associated with the MJO. The forcing data sets used in this study are available
648 from the National Center for Atmospheric Research Earth Observation Laboratory DYNAMO
649 archive (http://data.eol.ucar.edu/master_list/?project=DYNAMO).

650 Although the above results have yielded insight into the convective heating profiles and infer-
651 ences regarding cloud populations in the DYNAMO MJOs, further work is needed to directly
652 relate these findings to the research radar observations of precipitation systems at the S-PolKa site
653 on Gan Island, the TOGA radar on the R/V *Revelle*, and the 5-cm radar on the R/V *Mirai*, as
654 well as cloud radar observations on Gan Island. This work is currently underway. In addition, we
655 have not explored in this study the diurnal cycle of convection, which turns out to be particularly
656 important during the suppressed phases of the MJOs. A companion paper on this topic has been
657 submitted.

658 *Acknowledgments.* This research has been supported by the National Science Foundation under
659 Grants AGS-1059899, AGS-1138353, and AGS-1360237, the National Aeronautics and Space
660 Administration under Grant NNX13AF74G, and Department of Energy Grant DE-SC0008582.
661 Comments by Adam Sobel and two anonymous reviewers have led to considerable improvements

662 in the manuscript. We thank Zhe Feng of PNNL for generously providing the radiative heating
663 rates for Gan Island, ECMWF for making available its operational analyses, Thomas Birner and
664 Wayne Schubert for helpful discussions, and Rick Taft for assistance with preparation of figures.

665 **References**

- 666 Adler, R. F., and Coauthors, 2003: The Version 2 Global Precipitation Climatology Project
667 (GPCP) monthly precipitation analysis (1979-present). *J. Hydrometeor.*, **4**, 1147–1167.
- 668 Ao, C. O., T. K. Meehan, G. A. Hajj, A. J. Mannucci, and G. Beyerle, 2003: Lower-tropospheric
669 refractivity bias in GPS occultation retrievals. *J. Geophys. Res.*, **48**, doi:10.1029/2002JD003216.
- 670 Aonashi, K., and Coauthors, 2009: GSMaP passive, microwave precipitation retrieval algorithm:
671 Algorithm description and validation. *J. Meteor. Soc. Japan*, **87A**, 119–136.
- 672 Barnes, H. C., and R. A. Houze, Jr., 2013: The precipitating cloud population of the Madden-
673 Julian Oscillation over the Indian and west Pacific Ocean. *J. Geophys. Res.*, **118**, 6996–7023.
- 674 Benedict, J., and D. A. Randall, 2007: Observed characteristics of the MJO relative to maximum
675 rainfall. *J. Atmos. Sci.*, **64**, 2332–2354.
- 676 Chikira, M., 2014: Easward-propagating intraseasonal oscillation represented by Chikira-
677 Sugiyama cumulus parameterization. Part II: Understanding moisture variation under weak tem-
678 perature gradient balance. *J. Atmos. Sci.*, **71**, 615–639.
- 679 Ciesielski, P. E., L. Hartten, and R. H. Johnson, 1997: Impacts of merging profiler and rawinsonde
680 winds on TOGA COARE analyses. *J. Atmos. Oceanic Technol.*, **14**, 1264–1279.

681 Ciesielski, P. E., R. H. Johnson, P. T. Haertel, and J. Wang, 2003: Corrected TOGA COARE
682 sounding humidity data: Impact on diagnosed properties of convection and climate over the
683 warm pool. *J. Climate*, **16**, 2370–2384.

684 Ciesielski, P. E., R. H. Johnson, K. Yoneyama, and R. K. Taft, 2014b: Mitigation of Sri Lanka
685 island effects in Colombo sounding data its impact on DYNAMO analyses. *J. Meteor. Soc.
686 Japan*, (in press).

687 Ciesielski, P. E., and Coauthors, 2014a: Quality controlled upper-air sounding dataset for DY-
688 NAMO/CINDY/AMIE: Development and corrections. *J. Atmos. Oceanic Technol.*, **31**, 741–
689 764.

690 Del Genio, A. D., Y. Chen, D. Kim, and M.-S. Yao, 2012: The MJO transition from shallow to
691 deep convection in *cloudsat*/CALIPSO and GISS GCM simulations. *J. Climate*, **25**, 3755–3770.

692 DePasquale, A., C. Schumacher, and A. Rapp, 2014: Radar observations of MJO and Kelvin wave
693 interactions during DYNAMO/CINDY2011/AMIE. *J. Geophys. Res.*, **119**, 6347–6367.

694 Emanuel, K. A., and M. Bister, 1996: Moist convective velocity and buoyancy scales. *J. Atmos.
695 Sci.*, **53**, 3276–3285.

696 Fairall, C. W., E. F. Bradley, D. P. Rogers, J. B. Edson, and G. S. Young, 1996: Bulk parameteri-
697 zation of air-sea fluxes for TOGA COARE. *J. Geophys. Res.*, **101**, 3747–3764.

698 Feng, Z., S. A. McFarlane, C. Schumacher, S. Ellis, and N. Bharadwaj, 2014: Constructing a
699 merged cloud-precipitation radar dataset for tropical clouds during the DYNAMO/AMIE ex-
700 periment on Addu Atoll. *J. Atmos. Oceanic Technol.*, **31**, 1021–1042.

701 Figa-Saldaña, J., J. J. W. Wilson, E. Attema, R. Gelsthorpe, M. R. Drinkwater, and A. Stoffe-
702 len, 2002: The advanced scatterometer (ASCAT) on the meteorological operational (MetOp)
703 platform: A follow on for European wind scatterometers. *Can. J. Remote Sensing*, **28**, 404–412.

704 Funk, A., C. Schumacher, and J. Awaka, 2013: Analysis of rain classifications over the tropics by
705 Version 7 of the TRMM PR 2A23 algorithm. *J. Meteor. Soc. Japan*, **91**, 257–272.

706 Gosnell, R., C. W. Fairall, and P. J. Webster, 1995: The sensible heat of rainfall in the tropical
707 ocean. *J. Geophys. Res.*, **100**, 18 437–18 442.

708 Gottschalck, J., P. E. Roundy, C. J. S. III, A. Vintzileos, and C. Zhang, 2013: Large-scale atmo-
709 spheric and oceanic conditions during the 2011-12 DYNAMO field campaign. *Mon. Wea. Rev.*,
710 **141**, 4173–4196.

711 Haertel, P. T., G. N. Kiladis, A. Denno, and T. M. Rickenbach, 2008: Vertical-mode decomposi-
712 tions of 2-day waves and the Madden-Julian Oscillation. *J. Atmos. Sci.*, **65**, 813–833.

713 Hartmann, D. L., H. H. Hendon, and R. A. Houze, Jr., 1984: Some implications of the mesoscale
714 circulations in tropical cloud clusters for large-scale dynamics and climate. *J. Atmos. Sci.*, **41**,
715 113–121.

716 Hartmann, D. L., M. E. Ockert-Bell, and M. L. Michelsen, 1992: The effect of cloud type on the
717 Earth’s energy balance: Global analysis. *J. Climate*, **5**, 1281–1304.

718 Hohenegger, C., and B. Stevens, 2013: Preconditioning deep convection with cumulus congestus.
719 *J. Atmos. Sci.*, **70**, 448–464.

720 Holmlund, K., C. S. Velden, and M. Rohn, 2001: Enhanced automated quality control applied to
721 high-density satellite-derived winds. *Mon. Wea. Rev.*, **129**, 517–529.

722 Huffman, G. J., R. F. Adler, D. T. Bolvin, G. Gu, E. J. Nelkin, K. P. Bowman, E. F. Stocker, and
723 D. B. Wolff, 2007: The TRMM multi-satellite precipitation analysis: Quasi-global, multi-year,
724 combined-sensor precipitation estimates at fine scale. *J. Hydrometeor.*, **8**, 33–55.

725 Hung, M.-P., J.-L. Lin, W. Wang, D. Kim, T. Shinoda, and S. J. Weaver, 2013: MJO and con-
726 vectively coupled equatorial waves simulated by CMIP5 climate models. *J. Climate*, **26**, 6185–
727 6214.

728 Jiang, X., and Coauthors, 2011: Vertical diabatic heating structure of the MJO: Intercomparison
729 between recent reanalyses and TRMM. *Mon. Wea. Rev.*, **139**, 3208–3223.

730 Johnson, R. H., 1980: Diagnosis of convective and mesoscale motions during Phase III of GATE.
731 *J. Atmos. Sci.*, **37**, 733–753.

732 Johnson, R. H., and P. E. Ciesielski, 2000: Rainfall and radiative heating rate estimates from
733 TOGA COARE atmospheric budgets. *J. Atmos. Sci.*, **57**, 1497–1514.

734 Johnson, R. H., and P. E. Ciesielski, 2002: Characteristics of the 1998 summer monsoon onset
735 over the northern South China Sea. *J. Meteor. Soc. Japan*, **80**, 561–578.

736 Johnson, R. H., and P. E. Ciesielski, 2013: Structure and properties of Madden-Julian Oscillations
737 deduced from DYNAMO sounding arrays. *J. Atmos. Sci.*, **70**, 3157–3179.

738 Johnson, R. H., and X. Lin, 1987: Episodic trade wind regimes over the western Pacific warm
739 pool. *J. Atmos. Sci.*, **54**, 2020–2034.

740 Johnson, R. H., T. M. Rickenbach, S. A. Rutledge, P. E. Ciesielski, and W. H. Schubert, 1999:
741 Trimodal characteristics of tropical convection. *J. Atmos. Sci.*, **58**, 2729–2750.

742 Joyce, R. J., J. E. Janowiak, P. A. Arkin, and P. Xie, 2004: A method that produces global precipita-
743 tion estimates from passive microwave and infrared data at high spatial and temporal resolution.
744 *J. Hydrometeor.*, **5**, 487–503.

745 Katsumata, M., P. E. Ciesielski, and R. H. Johnson, 2011: Evaluation of budget analysis during
746 MISMO. *J. Appl. Meteor. Climatol.*, **40**, 241–254.

747 Kikuchi, K., and Y. N. Takayabu, 2004: The development of organized convection associated
748 with the MJO during TOGA COARE IOP: Trimodal characteristics. *Geophys. Res. Lett.*, **31**,
749 doi:10.1029/2004GL019601.

750 Kiladis, G. N., K. H. Straub, and P. T. Haertel, 2005: Zonal and vertical structure of the Madden-
751 Julian oscillation. *J. Atmos. Sci.*, **62**, 2790–2809.

752 Kiladis, G. N., K. H. Straub, G. C. Reid, and K. S. Gage, 2001: Aspects of interannual and
753 intraseasonal variability of the tropopause and lower stratosphere. *Quart. J. Roy. Meteor. Soc.*,
754 **127**, 1961–1984.

755 Kiladis, G. N., M. C. Wheeler, P. T. Haertel, K. H. Straub, and P. E. Roundy, 2009: Convectively
756 coupled equatorial waves. *Rev. Geophys.*, **47**, 2003, doi:10.1029/2008RG000266.

757 Kubota, T., and Coauthors, 2007: Global precipitation map using satellite-borne microwave ra-
758 diometers by the GSMaP project: Production and validation. *IEEE Trans. Geosci. Remote Sens.*,
759 **45**, 2259–2275.

760 Kumar, B. P., J. Vialard, M. Lengaigne, V. S. N. Murty, and M. J. McPhaden, 2012: TropFlux:
761 Air-sea fluxes for the global tropical oceans - Description and evaluation. *Clim. Dynam.*, **38**,
762 1521–1543.

763 Kuo, Y.-H., T.-K. Lee, S. Sokolovskiy, C. Rocken, W. Schreiner, D. Hunt, and R. A. Anthes,
764 2004: Inversion and error estimation of GPS radio occultation data. *J. Meteor. Soc. Japan*, **82**,
765 507–531.

766 L’Ecuyer, T. S., and G. McGarragh, 2010: A 10-year climatology of tropical radiative heating and
767 its vertical structure from TRMM observations. *J. Climate*, **23**, 519–541.

768 Lee, M.-I., I.-S. Kang, J.-K. Kim, and B. E. Mapes, 2001: Influence of cloud-radiation interaction
769 on simulating tropical intraseasonal oscillation with an atmosphere general circulation model.
770 *J. Geophys. Res.*, **106**, 14,291–14,233.

771 Lin, J.-L., and B. E. Mapes, 2004: Radiation budget of the tropical intraseasonal oscillation. *J.*
772 *Atmos. Sci.*, **61**, 2050–2062.

773 Lin, J.-L., B. E. Mapes, M. Zhang, and N. Newman, 2004: Stratiform precipitation, vertical heat-
774 ing profiles, and the Madden-Julian Oscillation. *J. Atmos. Sci.*, **61**, 296–309.

775 Lin, X., and R. H. Johnson, 1996: Heating, moistening, and rainfall over the western Pacific warm
776 pool during TOGA COARE. *J. Atmos. Sci.*, **53**, 3367–3383.

777 Liu, C., E. J. Zipser, and S. W. Nesbitt, 2007: Global distribution of tropical deep convection:
778 Different perspectives from TRMM infrared and radar data. *J. Climate*, **20**, 489–503.

779 Luo, H., and M. Yanai, 1984: The large-scale circulation and heat sources over the Tibetan Plateau
780 and surrounding areas during the early summer of 1979. part ii: Heat and moisture budgets.
781 *Mon. Wea. Rev.*, **112**, 966–989.

782 Madden, R. A., and P. R. Julian, 1972: Description of global-scale circulation cells in the tropics
783 with a 40-50 day period. *J. Atmos. Sci.*, **29**, 1109–1123.

784 Mapes, B. E., P. E. Ciesielski, and R. H. Johnson, 2003: Sampling errors in rawinsonde-array
785 budgets. *J. Atmos. Sci.*, **60**, 2697–2714.

786 Mapes, B. E., S. Tulich, J. Lin, and P. Zuidema, 2006: The mesoscale convection life cycle: Build-
787 ing block or prototype for large-scale tropical waves? *Dyn. Atmos. Oceans*, **42**, 3–29.

788 McNab, A. L., and A. K. Betts, 1978: Mesoscale budget study of cumulus convection. *Mon. Wea.*
789 *Rev.*, **106**, 1317–1331.

790 Neelin, J. D., and I. M. Held, 1997: Modeling tropical convergence based on the moist static
791 energy budget. *Mon. Wea. Rev.*, **115**, 3–12.

792 Ooyama, K., 1990: A thermodynamic foundation for modeling the moist atmosphere. *J. Atmos.*
793 *Sci.*, **47**, 2580–2593.

794 Powell, S. W., and R. A. Houze, Jr., 2013: The cloud population and the onset of the Madden-
795 Julian Oscillation over the Indian Ocean during DYNAMO-AMIE. *J. Geophys. Res.*, **118**,
796 11,979–11,995.

797 Randall, D. A., Harshvardhan, D. A. Dazlich, and T. G. Corsetti, 1989: Interactions among radi-
798 ation, convection, and large-scale dynamics in a general circulation model. *J. Atmos. Sci.*, **46**,
799 1943–1970.

800 Raymond, D. J., 2000: The Hadley circulation as a radiative-convective instability. *J. Atmos. Sci.*,
801 **57**, 1286–1297.

802 Raymond, D. J., 2001: A new model of the Madden-Julian oscillation. *J. Atmos. Sci.*, **58**, 2807–
803 2819.

804 Raymond, D. J., S. Sessions, A. H. Sobel, and Z. Fuchs, 2009: The mechanics of gross moist
805 stability. *J. Adv. Model. Earth Sys.*, **1**, 1–20.

806 Schumacher, C., and R. A. Houze, Jr., 2003: Stratiform rain in the tropics as seen by the TRMM
807 Precipitation Radar. *J. Climate*, **16**, 1739–1756.

808 Sherwood, S. C., V. Ramanathan, T. P. Barnett, M. K. Tyree, and E. Roeckner, 1994: Response
809 of an atmospheric general circulation model to radiative forcing of tropical clouds. *J. Geophys.*
810 *Res.*, **99**, 20 829–20 845.

811 Slingo, A., and J. M. Slingo, 1988: The response of a general circulation model to cloud longwave
812 radiative forcing. I: Introduction and initial experiments. *Quart. J. Roy. Meteor. Soc.*, **114**, 1027–
813 1962.

814 Slingo, A., and J. M. Slingo, 1991: The response of a general circulation model to cloud longwave
815 radiative forcing. II: Further studies. *Quart. J. Roy. Meteor. Soc.*, **117**, 333–364.

816 Sobel, A., and E. D. Maloney, 2012: An idealized semi-empirical framework for the Madden-
817 Julian oscillation. *J. Atmos. Sci.*, **69**, 1691–1705.

818 Sobel, A., and E. D. Maloney, 2013: Moisture modes and the eastward propagation of the MJO.
819 *J. Atmos. Sci.*, **70**, 187–192.

820 Sobel, A., S. Wang, and D. Kim, 2014: Moist static energy budget of the MJO during DYNAMO.
821 *J. Atmos. Sci.*, (in press).

822 Stephens, G. L., M. J. Webb, P. J. Minnett, P. H. Daum, L. Kleinman, I. Wittmeyer, and D. A.
823 Randall, 1994: Observations of the Earth’s radiation budget in relation to atmospheric hydrol-
824 ogy. 4: Atmospheric column radiative cooling over the world’s oceans. *J. Geophys. Res.*, **99**,
825 18,585–18,604.

826 Stephens, G. L., P. J. Webster, R. H. Johnson, R. Engelen, and T. S. L'Ecuyer, 2004: Observational
827 evidence for the mutual regulation of the tropical hydrological cycle and the tropical sea surface
828 temperatures. *J. Climate*, **17**, 2213–2224.

829 Tao, W.-K., C.-L. Shie, D. Johnson, S. Braun, R. H. Johnson, and P. E. Ciesielski, 2003: Convec-
830 tive systems over the South China Sea: Cloud-resolving model simulations. *J. Atmos. Sci.*, **60**,
831 2929–2956.

832 Thuburn, J., and G. C. Craig, 2002: On the temperature structure of the tropical stratosphere.
833 *J. Geophys. Res.*, **107**, ACL 10–1–ACL 10–10.

834 Trenberth, K. E., 1991: Climate diagnostics from global analyses: Conservation of mass in
835 ECMWF analyses. *J. Climate*, **4**, 707–722.

836 Tung, W.-W., C. Lin, B. Chen, M. Yanai, and A. Arakawa, 1999: Basic modes of cumulus heating
837 and drying observed during TOGA-COARE IOP. *Geophys. Res. Lett.*, **26**, 3117–3120.

838 Virts, K. S., and J. M. Wallace, 2010: Annual, interannual, and intraseasonal variability of tropical
839 tropopause transition layer cirrus. *J. Atmos. Sci.*, **67**, 3113–3129.

840 Virts, K. S., J. M. Wallace, Q. Fu, and T. P. Ackerman, 2010: Tropical tropopause transition layer
841 cirrus as represented by calipso lidar observations. *J. Atmos. Sci.*, **67**, 3097–3112.

842 Waite, M. L., and B. Khouider, 2010: The deepening of tropical convection by congestus precon-
843 ditioning. *J. Atmos. Sci.*, **67**, 2601–2615.

844 Wang, J., H. L. Cole, D. J. Carlson, E. R. Miller, K. Beierle, A. Paukkunen, and T. K. Laine, 2002:
845 Corrections of the humidity measurement errors from the vaisala rs80 radiosonde—Application
846 to TOGA COARE data. *J. Atmos. Oceanic Technol.*, **19**, 981–1002.

- 847 Webster, P. J., 1994: TOGA COARE: The role of hydrological processes in ocean-atmosphere
848 interaction. *Rev. Geophys.*, **32**, 427–476.
- 849 Webster, P. J., and R. Lukas, 1992: TOGA COARE: The coupled ocean-atmosphere response
850 experiment. *Bull. Amer. Meteor. Soc.*, **73**, 1377–1416.
- 851 Weller, R. A., and S. P. Anderson, 1996: Surface meteorology and air-sea fluxes in the western
852 equatorial Pacific warm pool during the TOGA Coupled Ocean-Atmosphere Response Experi-
853 ment. *J. Climate*, **9**, 1959–1990.
- 854 Wheeler, M. C., and H. H. Hendon, 2004: An all-season real-time multivariate MJO index: De-
855 velopment of an index for monitoring and prediction. *Mon. Wea. Rev.*, **132**, 1917–1932.
- 856 Wielicki, B. A., B. R. Barkstrom, E. F. Harrison, R. B. Lee, III, G. L. Smith, and J. E. Cooper, 1996:
857 Clouds and the earth’s radiant energy system (CERES): An earth observing system experiment.
858 *Bull. Amer. Meteor. Soc.*, **77**, 853–868.
- 859 Wu, X., M. W. Moncrieff, and K. A. Emanuel, 2000: Evaluation of large-scale forcing during
860 TOGA COARE for cloud-resolving models and single-column models. *J. Atmos. Sci.*, **57**, 2977–
861 2985.
- 862 Xu, W., and S. A. Rutledge, 2014: Convective characteristics of the Madden-Julian Oscillation
863 over the Central Indian Ocean observed by shipborne radar during DYNAMO. *J. Atmos. Sci.*,
864 **71**, 2859–2877.
- 865 Yanai, M., S. Esbensen, and J.-H. Chu, 1973: Determination of bulk properties of tropical cloud
866 clusters from large-scale heat and moisture budgets. *J. Atmos. Sci.*, **30**, 611–627.

- 867 Yanai, M., and R. H. Johnson, 1993: Impacts of cumulus convection on thermodynamic fields.
868 *The representation of cumulus convection in numerical models*, No. 46, Meteor. Monogr., Amer.
869 Meteor. Soc., 39–62.
- 870 Yoneyama, K., C. Zhang, and C. N. Long, 2013: Tracking pulses of the Madden-Julian Oscillation.
871 *Bull. Amer. Meteor. Soc.*, **94**, 1871–1891.
- 872 Yoneyama, K., and Coauthors, 2008: MISMO field experiment in the equatorial Indian Ocean.
873 *Bull. Amer. Meteor. Soc.*, **89**, 1889–1903.
- 874 Yu, J.-Y., C. Chou, and J. D. Neelin, 1998: Estimating the gross moist stability of the tropical
875 atmosphere. *J. Atmos. Sci.*, **55**, 1354–1372.
- 876 Yu, L., and R. A. Weller, 2007: Objectively analyzed air-sea heat fluxes for the global oceans
877 (1981-2005). *Bull. Amer. Meteor. Soc.*, **88**, 527–539.
- 878 Yuan, J., and R. A. Houze, Jr., 2013: Deep convective systems observed by A-Train in the tropical
879 Indo-Pacific region affected by the MJO. *J. Atmos. Sci.*, **70**, 465–486.
- 880 Zhang, C., 2005: Madden-Julian Oscillation. *Rev. Geophys.*, **89**, 2003, doi:10.1029/
881 2004RG000158.
- 882 Zhang, C., 2013: The Madden-Julian Oscillation: Bridging weather and climate. *Bull. Amer. Me-*
883 *eteor. Soc.*, **94**, 1849–1870.
- 884 Zhang, C., J. Gottschalk, E. D. Maloney, M. W. Moncrieff, F. Vitart, D. E. Waliser, B. Wang,
885 and M. C. Wheeler, 2013: Cracking the MJO nut. *Geophys. Res. Lett.*, **40**, 1223–1230, doi:
886 10.1002/grl.50244,2013.

887 Zuluaga, M. D., and R. A. Houze, Jr., 2013: Evolution of the population of precipitating convective
888 systems over the Equatorial Indian Ocean in active phases of the Madden-Julian Oscillation. *J.*
889 *Atmos. Sci.*, **70**, 2713–2725.

890 **LIST OF TABLES**

891 **Table 1.** SOP-mean rainfall and radiative heating rates based on budgets and satellite
892 estimates for DYNAMO NSA and SSA, as well as comparisons with four-
893 month budget averages for TOGA COARE Intensive Flux Array (IFA). Areas
894 of arrays are also indicated. 44

895 TABLE 1. SOP-mean rainfall and radiative heating rates based on budgets and satellite estimates for DY-
 896 NAMO NSA and SSA, as well as comparisons with four-month budget averages for TOGA COARE Intensive
 897 Flux Array (IFA). Areas of arrays are also indicated.

Item	Source	DYNAMO NSA	DYNAMO SSA	COARE IFA
Areas		(700 km) ²	(830 km) ²	(474 km) ²
Rainfall rates (mm day ⁻¹)				
	<i>Q</i> ₂ budget	9.4	10.6	8.4
	TRMM	8.9	9.1	
	CMORPH	9.3	9.7	
	GPCP	9.8	9.2	
	GSMaP	9.2	8.2	
Tropospheric-mean radiative heating $\langle Q_R \rangle$ (K day ⁻¹)				
	Budgets without rain correction	-0.53	-0.46	
	Budgets with rain correction	-0.59	-0.53	-0.55
	CERES	-0.63	-0.61	

LIST OF FIGURES

895		
896	Fig. 1.	DYNAMO/CINDY/AMIE sounding network for the period October-December 2011. Analysis domain includes high-frequency soundings (4 and 8 per day; yellow and red dots, respectively) and operational sounding sites (1 or 2 per day; black dots). Data from R/V <i>Sagar Kanya</i> (<i>S. K.</i>) and R/V <i>Baruna Jaya</i> (<i>B. J.</i>), which were on station for brief periods (25 September-19 October for <i>S. K.</i> and 5-18 December for <i>B. J.</i>), were also utilized in the analyses. Sites with enhanced sounding frequency during the Special Observing Period are labeled. 47
897		
898		
899		
900		
901		
902		
903	Fig. 2.	(Upper three panels) Time series of daily-averaged sensible and latent heat fluxes (W m^{-2}), and SST ($^{\circ}\text{C}$) from TropFlux (black curves: means within 1° radius of <i>Revelle's</i> nominal position) and the R/V <i>Revelle</i> (red pluses). (Lower panel) Average rainfall rate (mm day^{-1}) within a 1° radius of <i>Revelle</i> nominal position (Eq., 80.5°E) from TRMM 3B42. Mean values for TropFlux (black) and the <i>Revelle</i> (red) are in parentheses. 48
904		
905		
906		
907		
908	Fig. 3.	Time-longitude plot of rainfall rates from TRMM 3B42 (3-hourly values, color) and moisture budget (3-day running mean filtering of daily-average values, contours) (mm day^{-1}) averaged 5°N to 5°S for DYNAMO SOP. Vertical dashed lines denote east and west boundaries of sounding arrays. Missing moisture budget results between 95 and 100°E marks location of Sumatra, where surface flux data do not exist. 49
909		
910		
911		
912		
913	Fig. 4.	Mean rainfall rate (mm day^{-1}) over Indian Ocean for October-November 2011 from (upper) TRMM 3B42 product and (lower) moisture budget. White lines denote sounding arrays. Budget rainfall not computed over land due to the absence of surface flux data there. 50
914		
915		
916	Fig. 5.	Time series for October and November of daily-average values of (upper) apparent heat source Q_1 (K day^{-1}), (middle) apparent moisture sink Q_2 , and (lower) TRMM 3B42v7 rainfall rate (mm day^{-1}) for NSA. Wheeler and Hendon (2004) RMM index shown at bottom. Shaded bar denotes port call period for R/V <i>Revelle</i> 51
917		
918		
919		
920	Fig. 6.	As in Fig. 5, except for SSA. Dark and light vertical shaded bars indicate times when R/V <i>Mirai</i> and <i>Revelle</i> , respectively, were off station. 52
921		
922	Fig. 7.	(left and center panels) Frequency-altitude distributions and (right panel) SOP-mean profiles of Q_1 and Q_2 for (top) NSA and (bottom) SSA for October-November 2011. 53
923		
924	Fig. 8.	SOP time series (filtered, 3-day running mean) for NSA of (upper) rainfall rate (mm day^{-1}) computed from Q_2 budget with (green curve) and without (red curve) inclusion of ECMWF OA, with comparison to TRMM 3B42v7 data (black curve); and (lower) changes to Q_2 budget resulting from inclusion of model reanalyses. Numbers in parentheses refer to SOP-mean rainfall rate. Shading denotes period of R/V <i>Revelle</i> port call. 54
925		
926		
927		
928		
929	Fig. 9.	SOP time series of 3-day running mean filtered rainfall rate (mm day^{-1}) computed from Q_2 budget (with ECMWF OA included) compared to TRMM 3B42v7, CMORPH, GPCP, and GSMaP estimates for (upper) NSA and (lower) SSA. Numbers in parentheses refer to SOP-mean rainfall rates. Light (dark) shading denotes periods of R/V <i>Revelle</i> (<i>Mirai</i>) port calls. RMM index shown at bottom. 55
930		
931		
932		
933		
934	Fig. 10.	(left) Time series of daily-averaged net radiative heating rate (K day^{-1}) at Gan Island from PNNL CombRet product and (right) mean profiles of shortwave (SW), longwave (LW) and net radiative heating rates for 10 October – 31 December 2011. 56
935		
936		

937 **Fig. 11.** SOP time series (3-day running mean filtered, daily-average values) of net radiative heating
938 rate (K day^{-1}) from budgets and CERES product for array areas, and from PNNL CombRet
939 product for Gan Island, for (upper) NSA and (lower) SSA. Solid (dashed) black curves are
940 $\langle Q_R \rangle$ with (without) inclusion of terms involving the effects of rain (see text). Numbers
941 in parentheses are SOP-mean values. Light (dark) shading denotes periods of R/V *Revelle*
942 (*Mirai*) port calls. 57

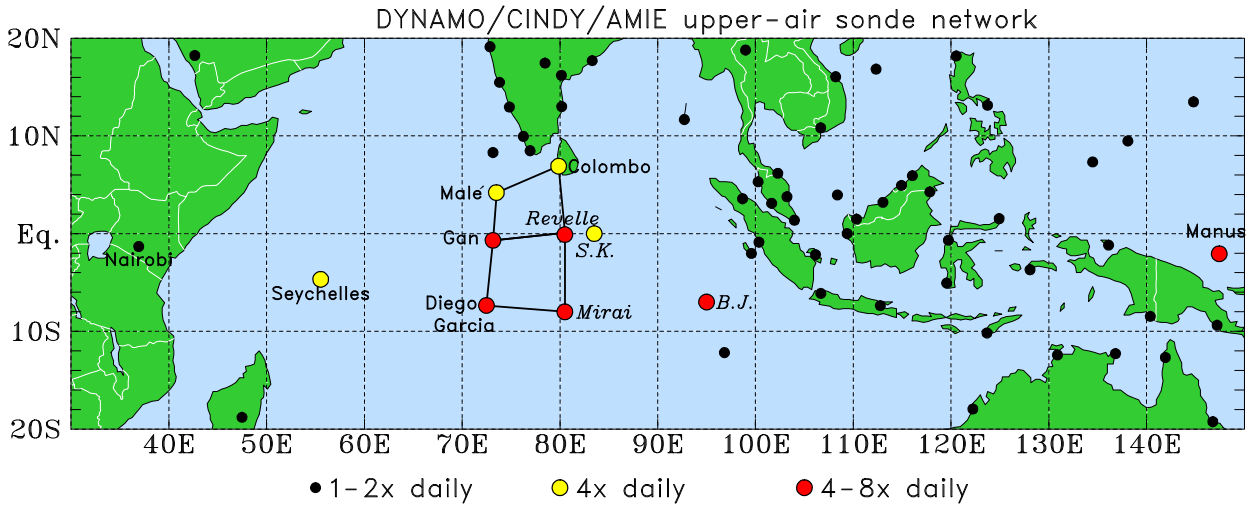
943 **Fig. 12.** October 1 – December 6 time series (3-day running mean filtered, daily-average values)
944 of (upper) relative humidity (%), with respect to ice for $T < 0^\circ\text{C}$); (middle) $\langle Q_R \rangle$ from
945 budgets (black) and CERES (red); and (lower) cloud fractional area from CERES for the
946 following definitions of cloud layers: low ($p > 700$ hPa), med-low ($700 \text{ hPa} > p > 500$
947 hPa), med-hi ($500 \text{ hPa} > p > 300$ hPa), and high ($p < 300$ hPa) for NSA. Shaded region
948 denotes period when R/V *Revelle* was off station. RMM index shown at bottom. 58

949 **Fig. 13.** (upper) Comparison of anomalies of CERES $\langle Q_R \rangle$ and convective heating $\langle Q_{conv} \rangle$
950 for NSA for DYNAMO SOP based on 3-day running mean filtered, daily-averaged values.
951 (middle) Time series of ratio of cloud radiative forcing $\langle Q_R \rangle_{CF}$ to $\langle Q_{conv} \rangle$. Values
952 plotted only when daily TRMM precipitation exceeded 1 mm day^{-1} . (lower) TRMM 3B42
953 rainfall rate (mm day^{-1}) time series for NSA. Shaded region denotes period when R/V
954 *Revelle* was off station. 59

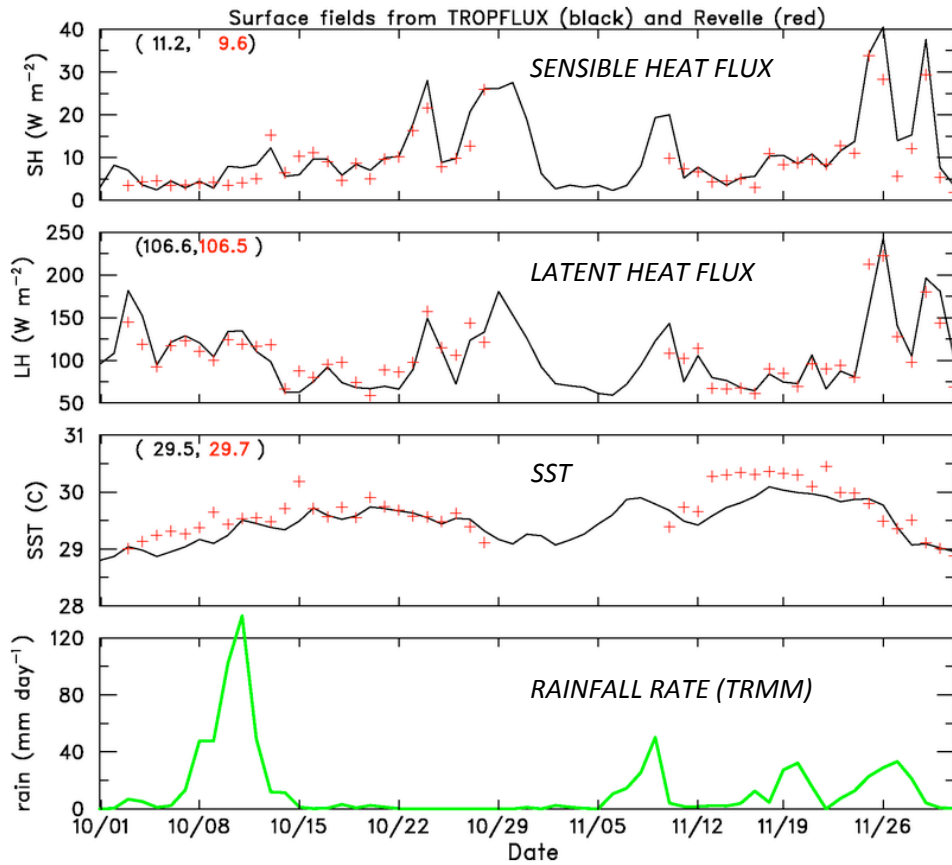
955 **Fig. 14.** Time series of daily-average values of (upper) vertical eddy moist static energy flux F
956 (contours: 50 W m^{-2} intervals; shading denotes gradations between intervals) and (lower)
957 TRMM 3B42v7 rainfall rate (mm day^{-1}) for NSA for DYNAMO SOP. Shaded region de-
958 notes period when R/V *Revelle* was off station. RMM index shown at bottom. 60

959 **Fig. 15.** As in Fig. 14, except for SSA. Dark and light vertical shaded bars indicate times when R/V
960 *Mirai* and *Revelle*, respectively, were off station. 61

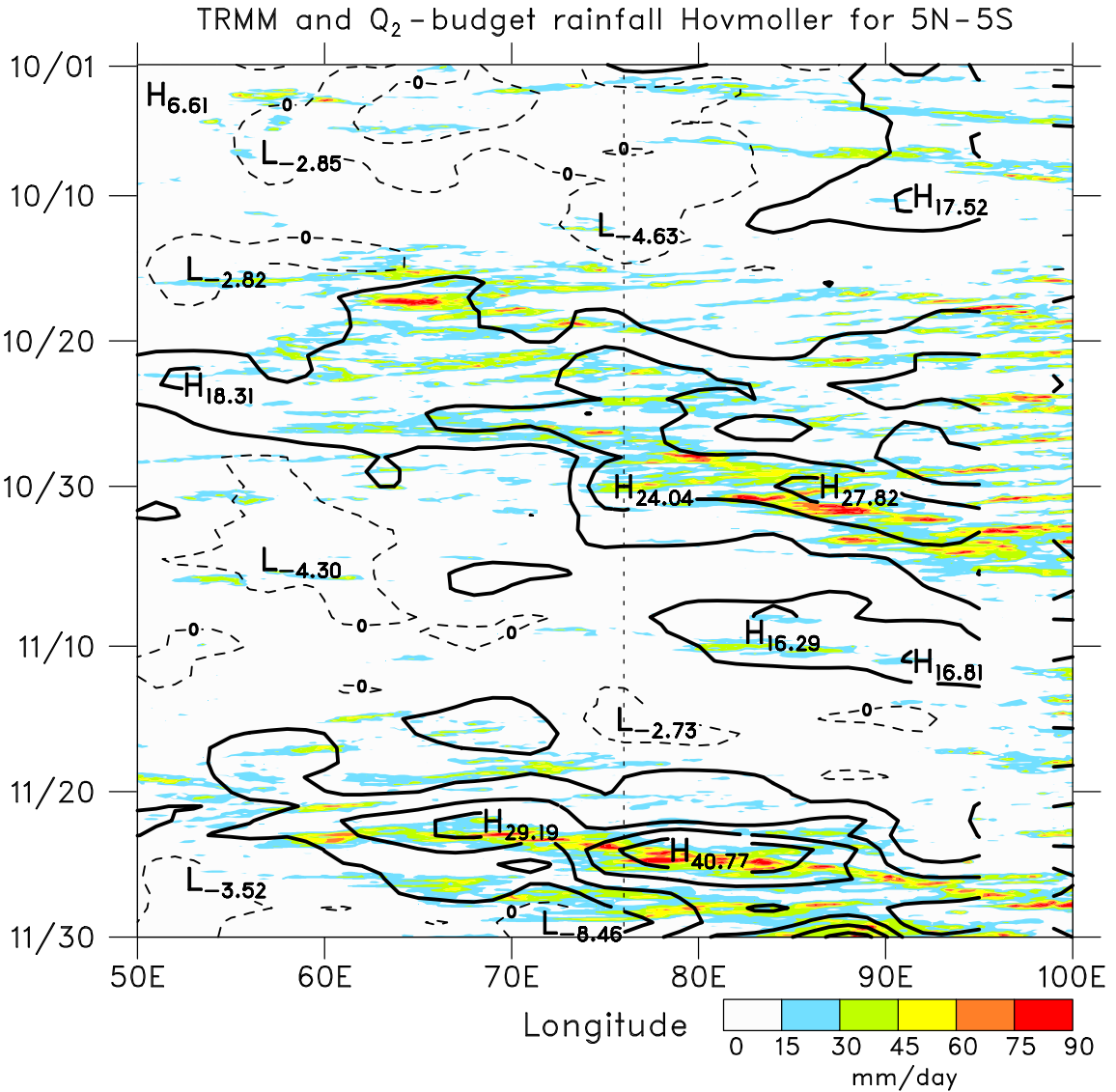
961 **Fig. 16.** (upper left) SOP-mean profiles of $Q_1 - Q_2 - Q_R$ (K day^{-1}) for NSA and SSA and (upper
962 right) SSA minus NSA difference in those quantities. (lower left) F (W m^{-2}) for NSA and
963 SSA and (lower right) SSA minus NSA difference in F . Surface sensible plus latent heat
964 flux (F_0) from TropFlux is indicated by asterisks on bottom lower-left axis for NSA (black)
965 and SSA (red). 62



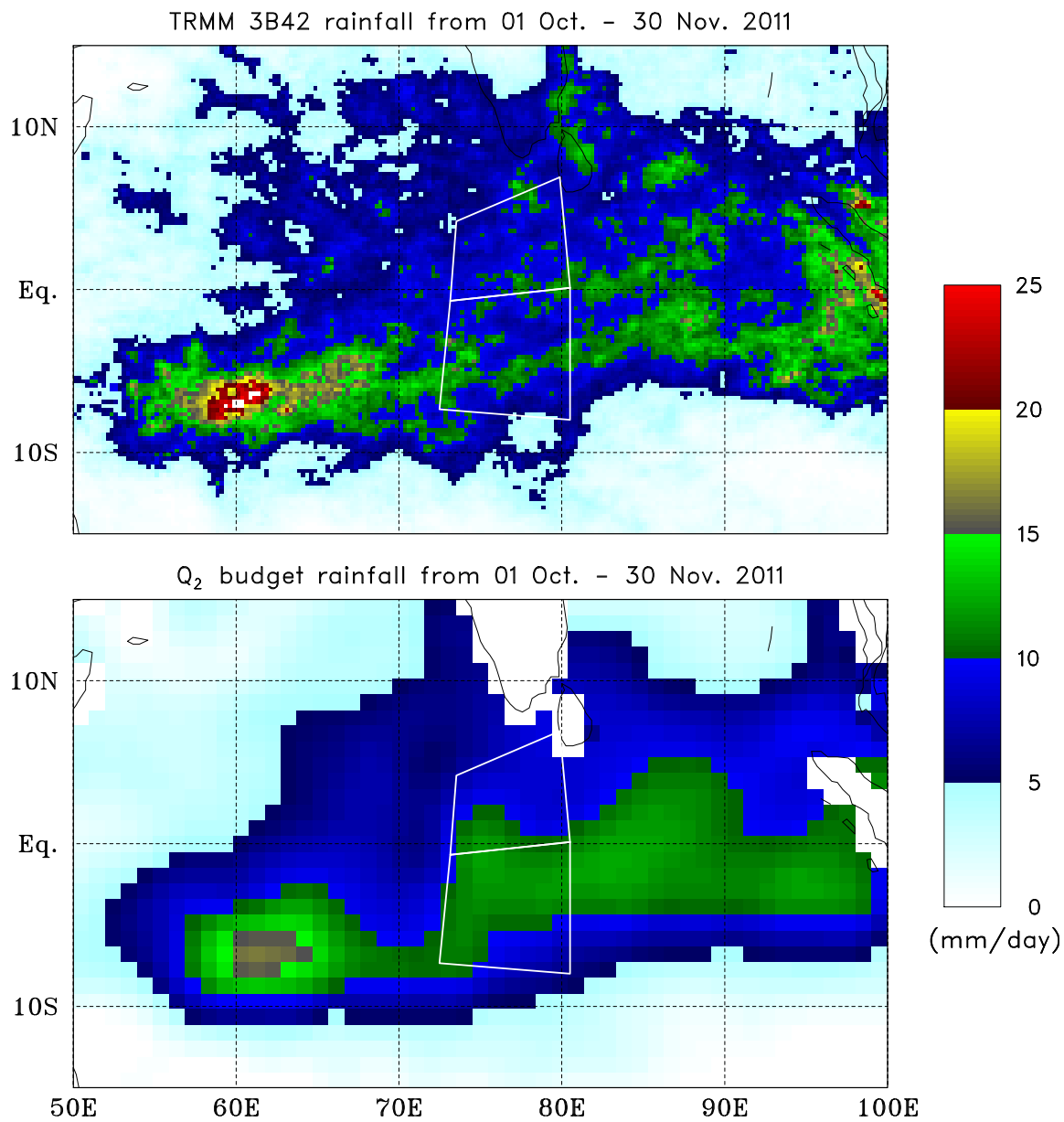
966 FIG. 1. DYNAMO/CINDY/AMIE sounding network for the period October-December 2011. Analysis do-
 967 main includes high-frequency soundings (4 and 8 per day; yellow and red dots, respectively) and operational
 968 sounding sites (1 or 2 per day; black dots). Data from R/V *Sagar Kanya* (*S. K.*) and R/V *Baruna Jaya* (*B. J.*),
 969 which were on station for brief periods (25 September-19 October for *S. K.* and 5-18 December for *B. J.*), were
 970 also utilized in the analyses. Sites with enhanced sounding frequency during the Special Observing Period are
 971 labeled.



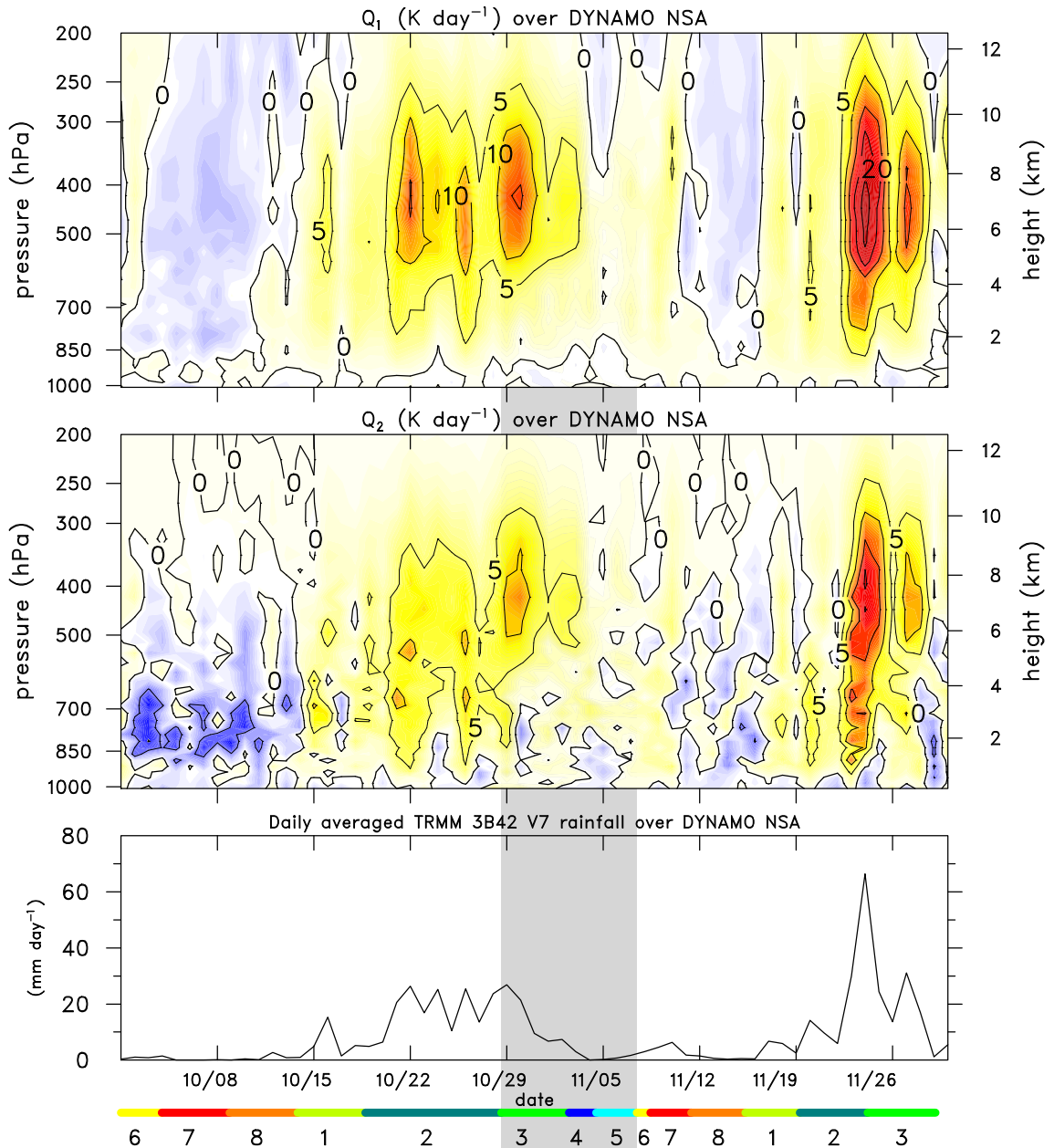
966 FIG. 2. (Upper three panels) Time series of daily-averaged sensible and latent heat fluxes (W m^{-2}), and SST
 967 ($^{\circ}\text{C}$) from TropFlux (black curves: means within 1° radius of *Reville's* nominal position) and the R/V *Reville*
 968 (red pluses). (Lower panel) Average rainfall rate (mm day^{-1}) within a 1° radius of *Reville* nominal position
 969 (Eq., 80.5°E) from TRMM 3B42. Mean values for TropFlux (black) and the *Reville* (red) are in parentheses.



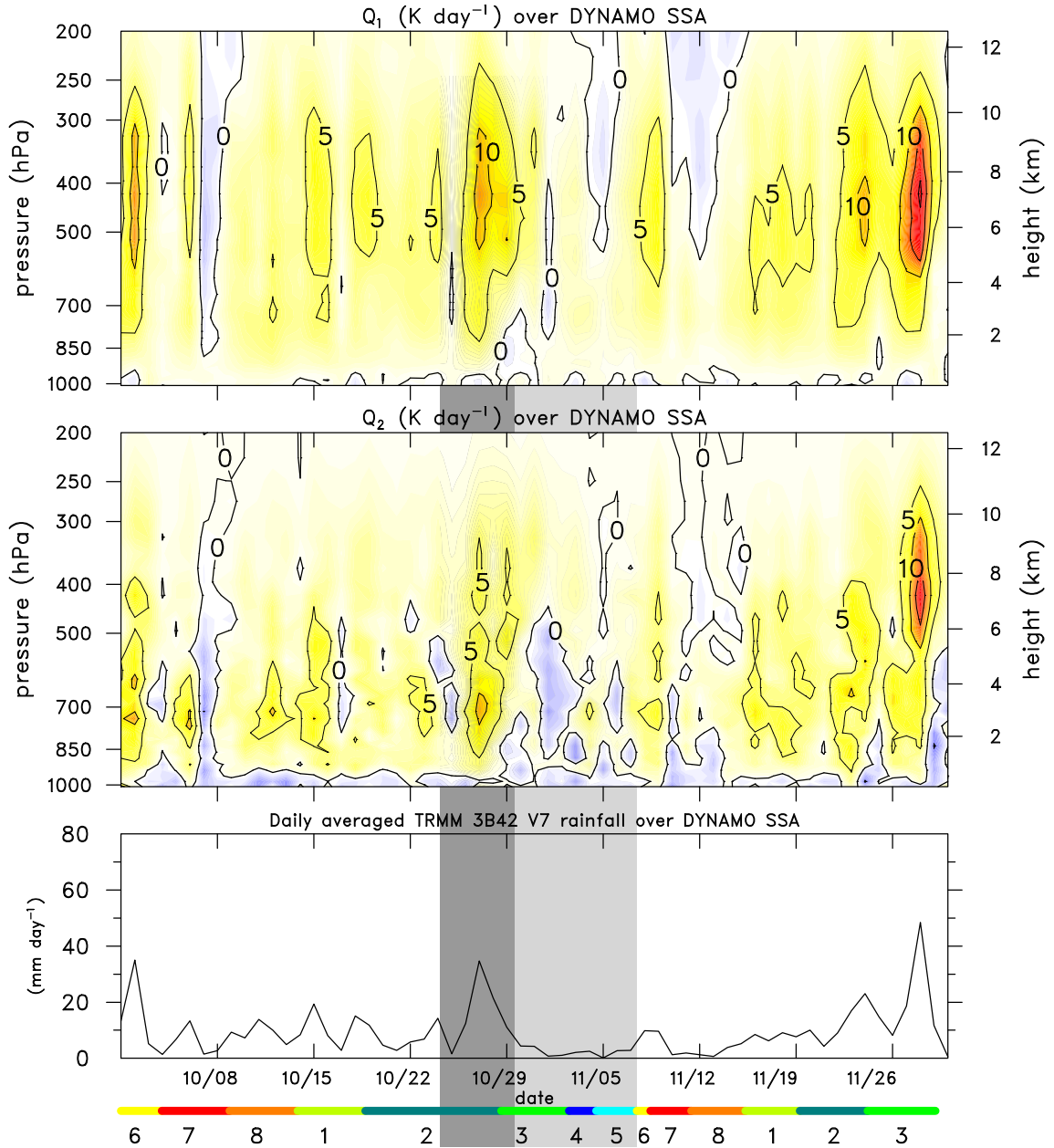
966 FIG. 3. Time-longitude plot of rainfall rates from TRMM 3B42 (3-hourly values, color) and moisture budget
 967 (3-day running mean filtering of daily-average values, contours) (mm day^{-1}) averaged 5°N to 5°S for DYNAMO
 968 SOP. Vertical dashed lines denote east and west boundaries of sounding arrays. Missing moisture budget results
 969 between 95 and 100°E marks location of Sumatra, where surface flux data do not exist.



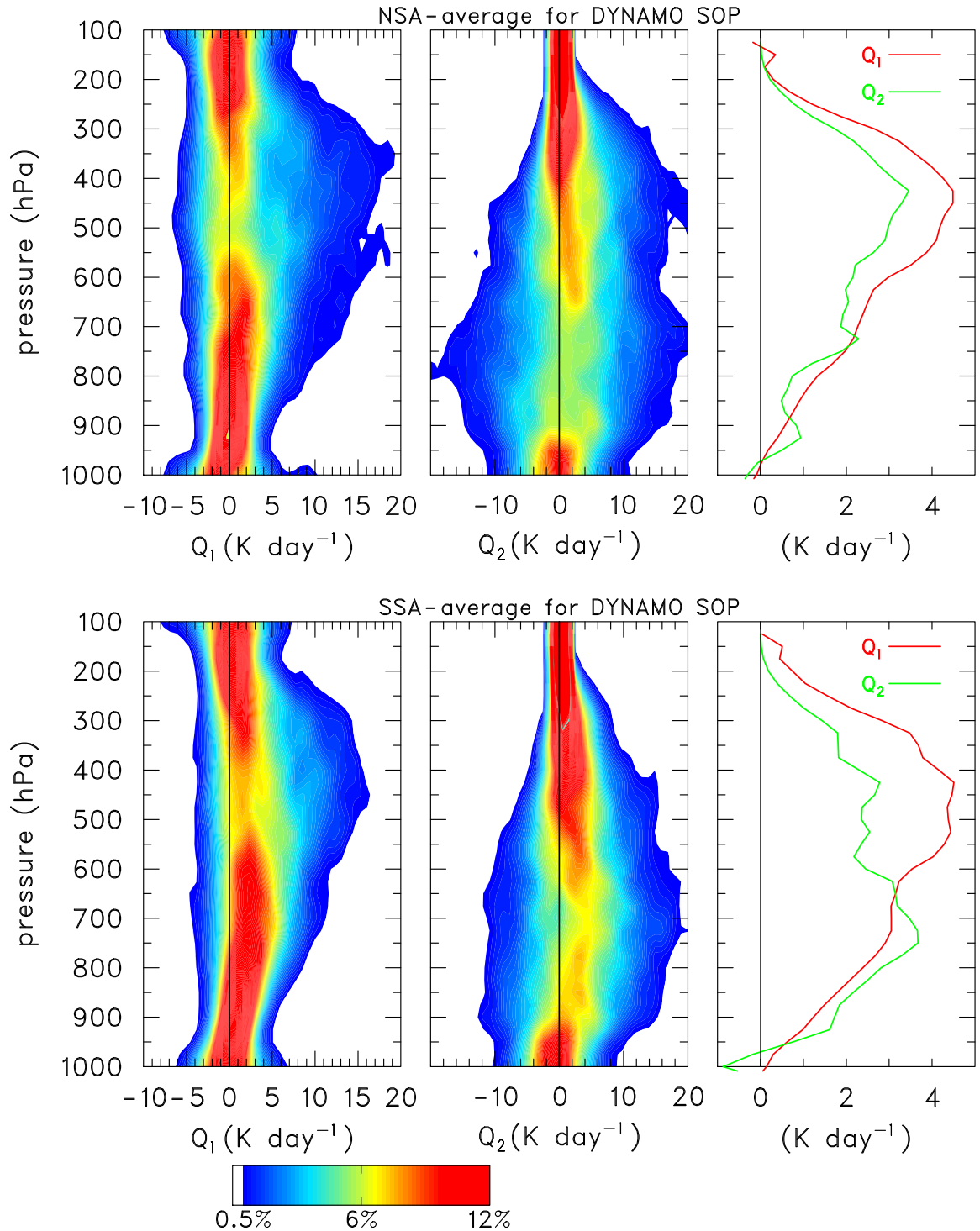
966 FIG. 4. Mean rainfall rate (mm day^{-1}) over Indian Ocean for October-November 2011 from (upper) TRMM
 967 3B42 product and (lower) moisture budget. White lines denote sounding arrays. Budget rainfall not computed
 968 over land due to the absence of surface flux data there.



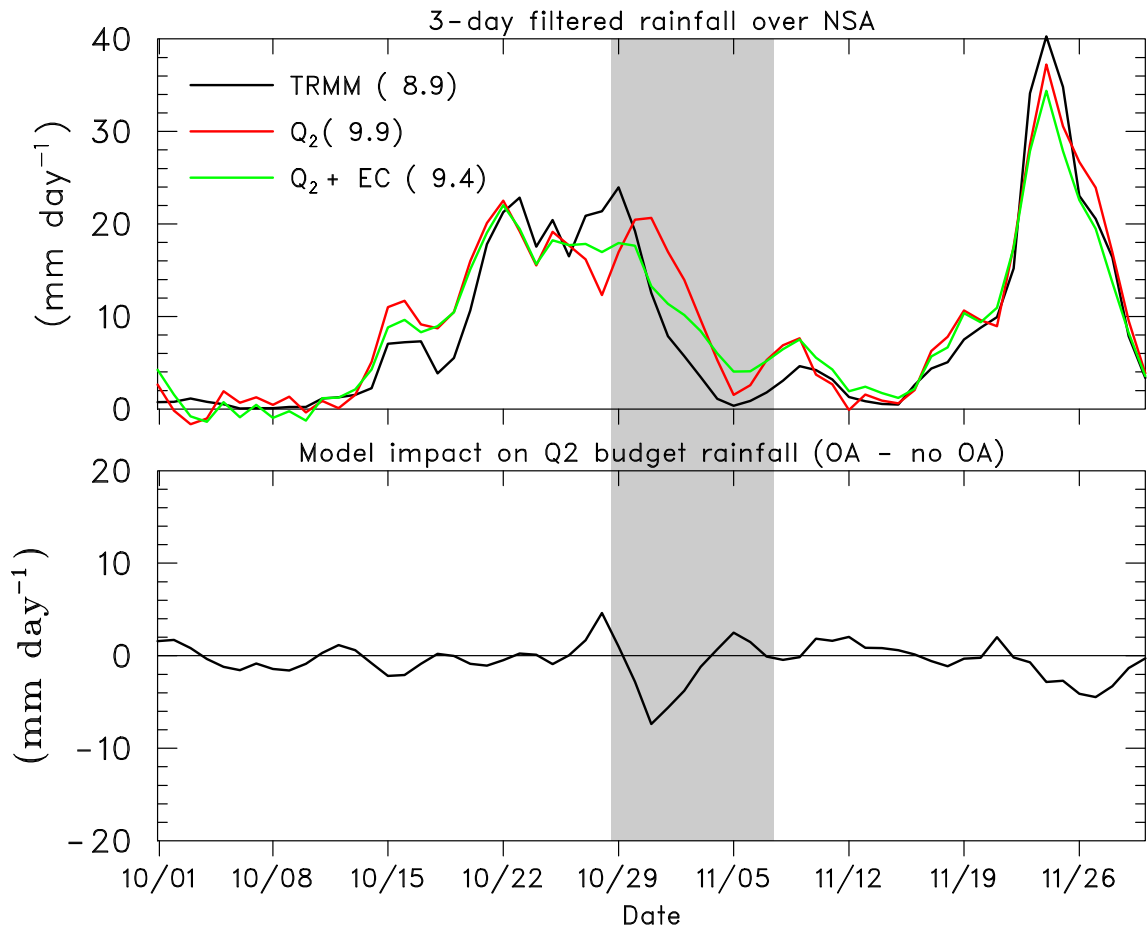
966 FIG. 5. Time series for October and November of daily-average values of (upper) apparent heat source Q_1
 967 (K day^{-1}), (middle) apparent moisture sink Q_2 , and (lower) TRMM 3B42v7 rainfall rate (mm day^{-1}) for NSA.
 968 Wheeler and Hendon (2004) RMM index shown at bottom. Shaded bar denotes port call period for R/V *Revelle*.



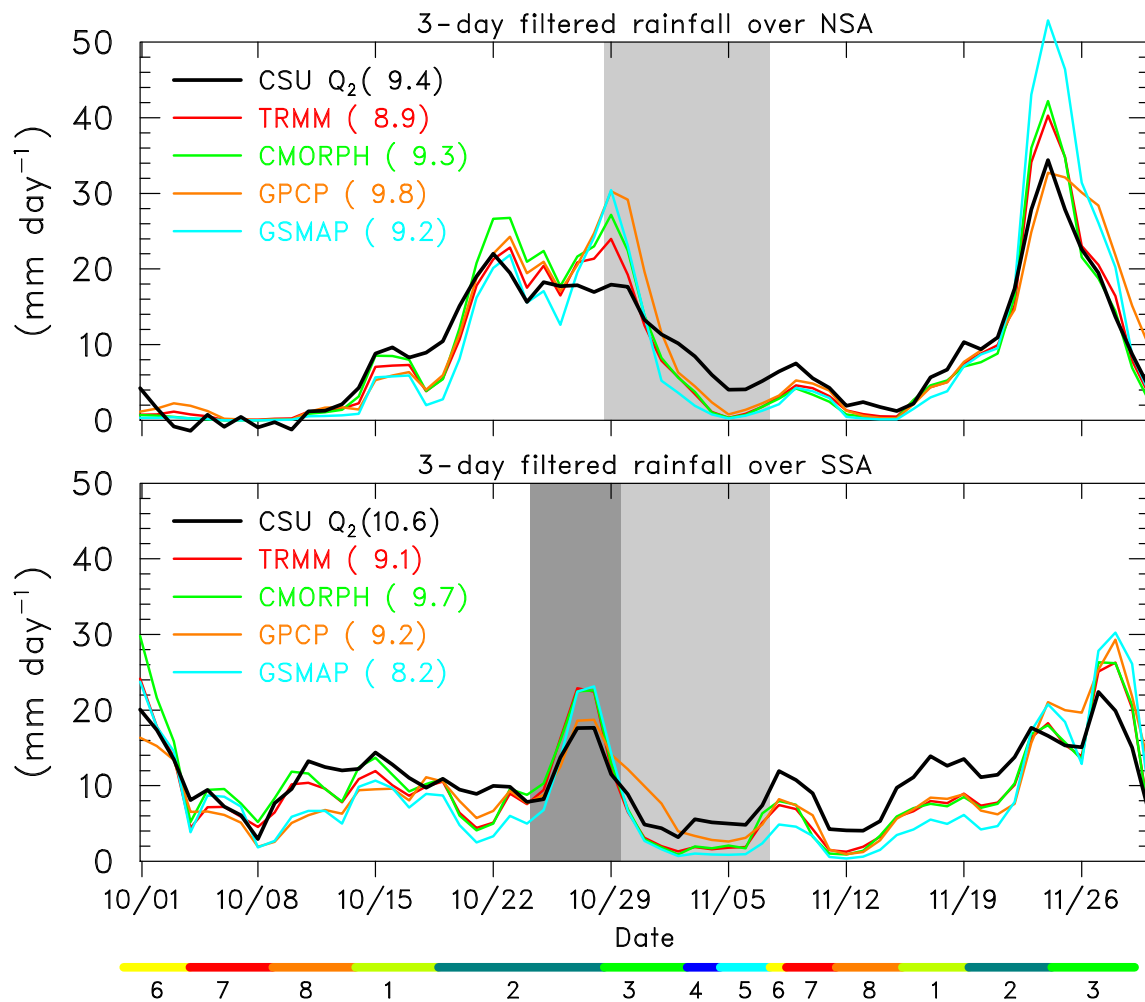
966 FIG. 6. As in Fig. 5, except for SSA. Dark and light vertical shaded bars indicate times when R/V *Mirai* and
 967 *Revelle*, respectively, were off station.



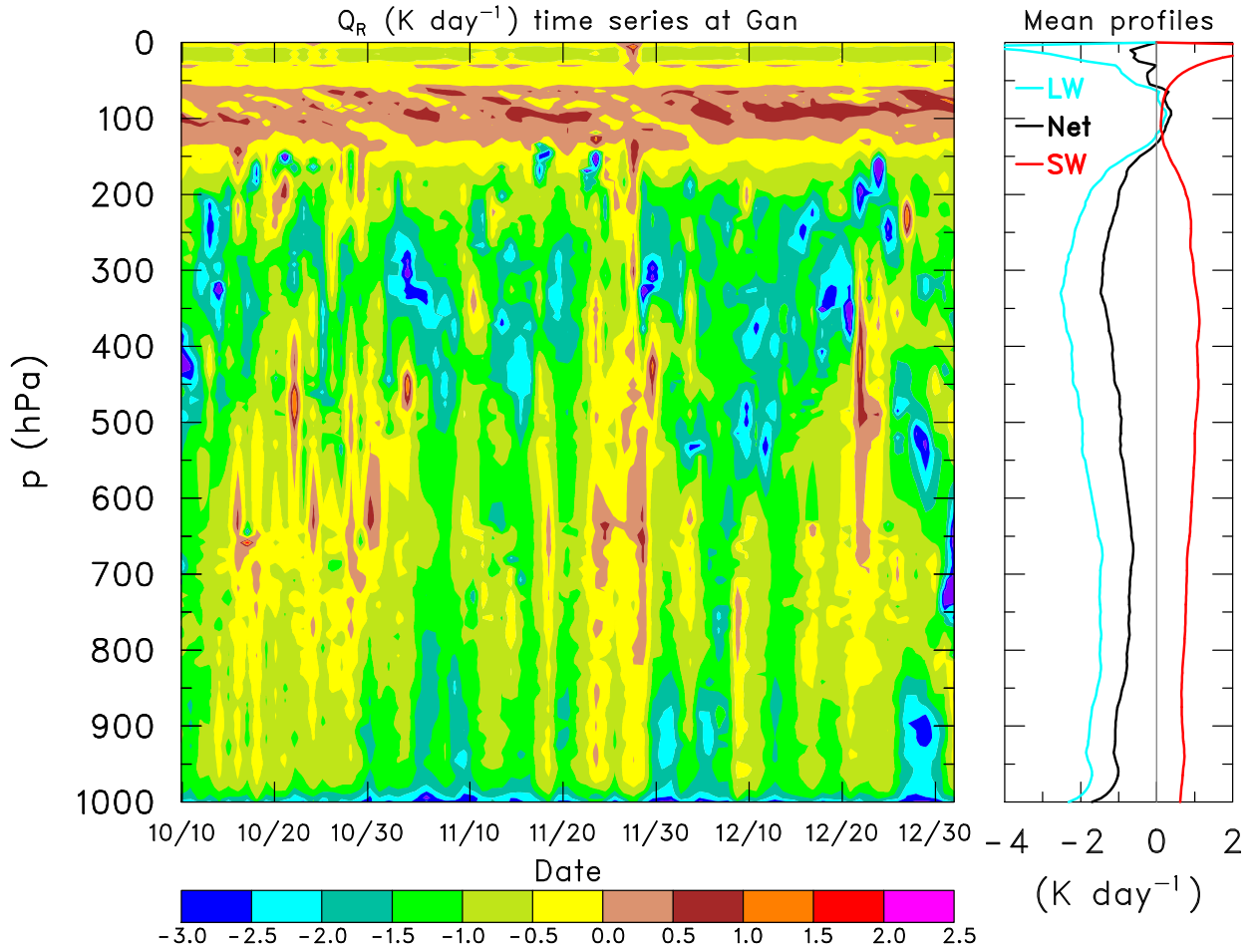
966 FIG. 7. (left and center panels) Frequency-altitude distributions and (right panel) SOP-mean profiles of Q_1
 967 and Q_2 for (top) NSA and (bottom) SSA for October-November 2011.



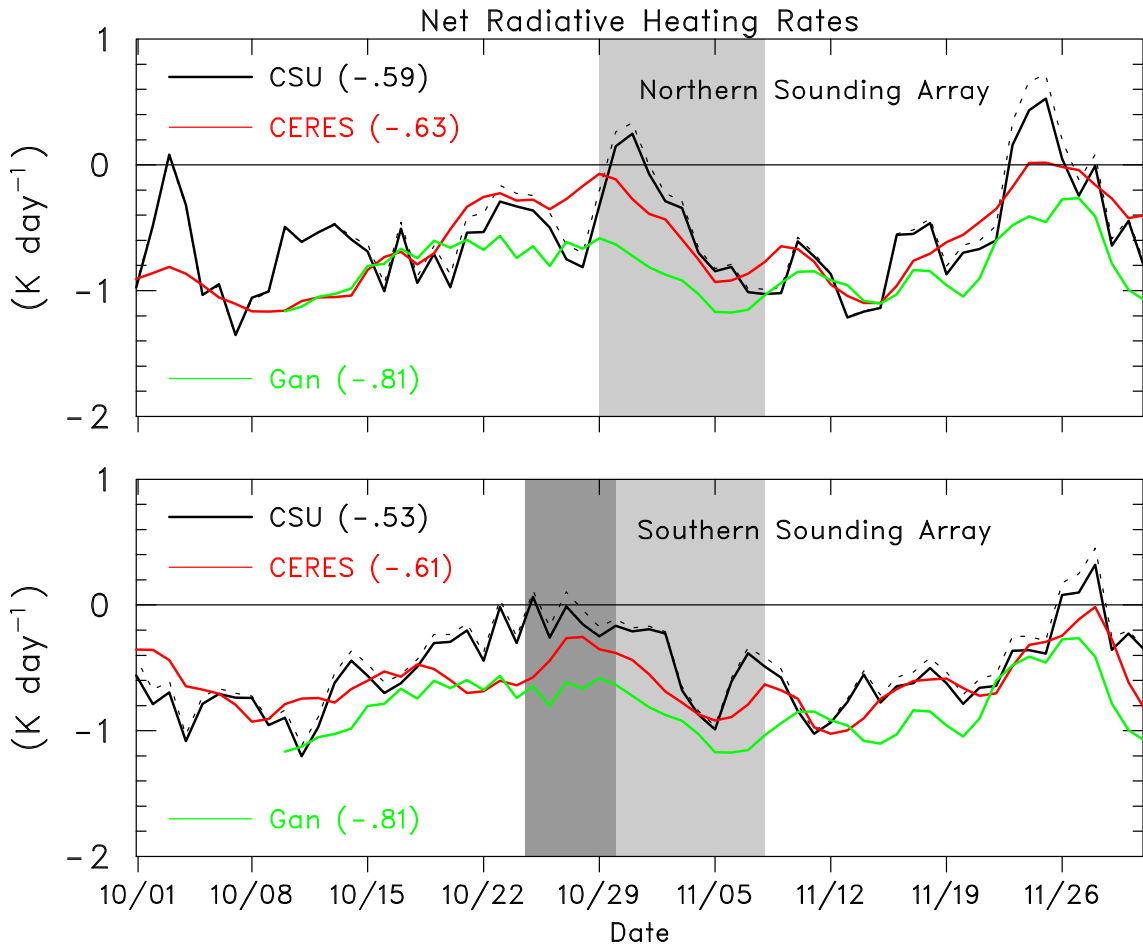
966 FIG. 8. SOP time series (filtered, 3-day running mean) for NSA of (upper) rainfall rate (mm day^{-1}) com-
 967 puted from Q_2 budget with (green curve) and without (red curve) inclusion of ECMWF OA, with comparison
 968 to TRMM 3B42v7 data (black curve); and (lower) changes to Q_2 budget resulting from inclusion of model re-
 969 analyses. Numbers in parentheses refer to SOP-mean rainfall rate. Shading denotes period of R/V *Revelle* port
 970 call.



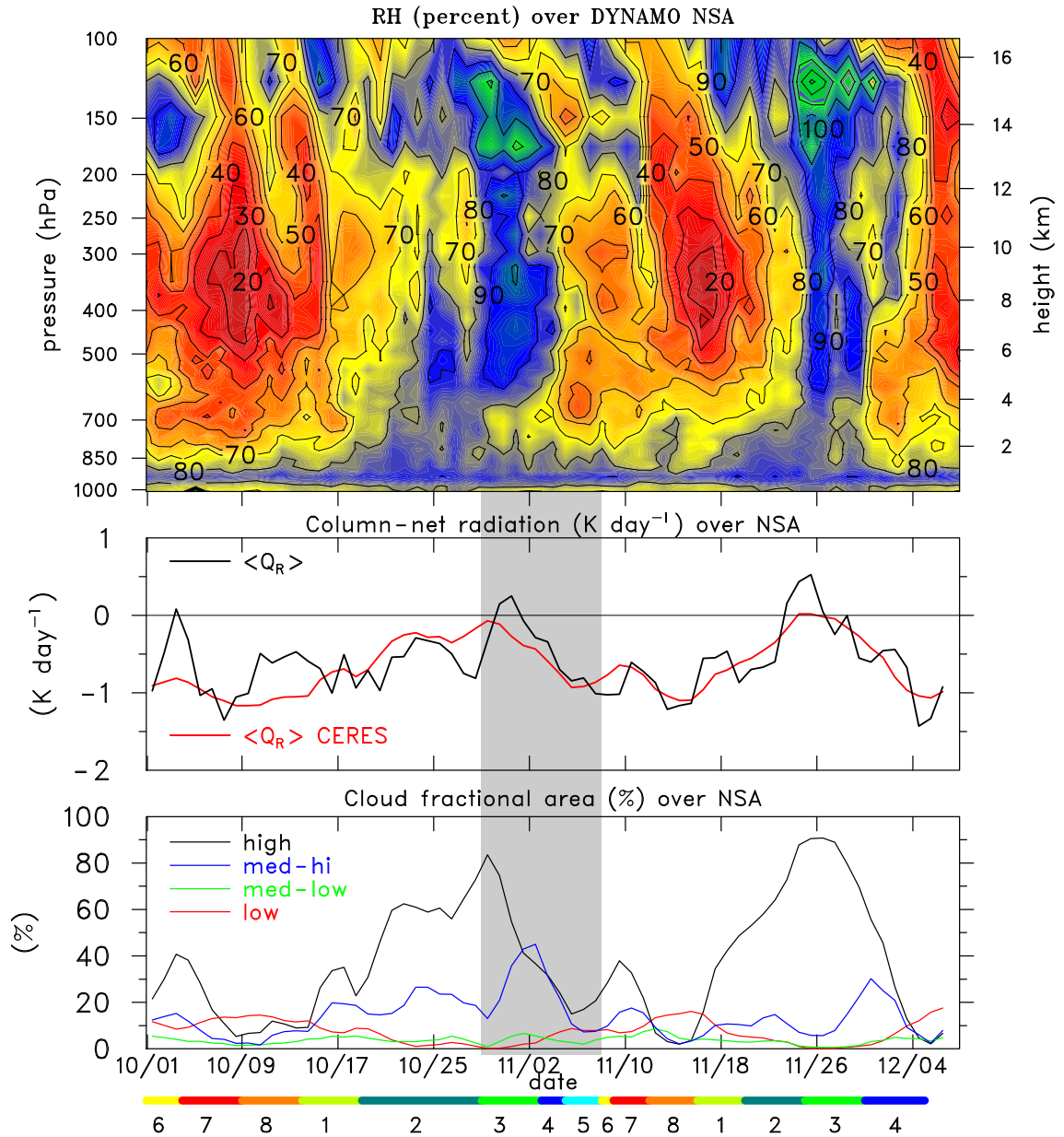
966 FIG. 9. SOP time series of 3-day running mean filtered rainfall rate (mm day^{-1}) computed from Q_2 budget
 967 (with ECMWF OA included) compared to TRMM 3B42v7, CMORPH, GPCP, and GSMaP estimates for (upper)
 968 NSA and (lower) SSA. Numbers in parentheses refer to SOP-mean rainfall rates. Light (dark) shading denotes
 969 periods of R/V *Revelle* (*Mirai*) port calls. RMM index shown at bottom.



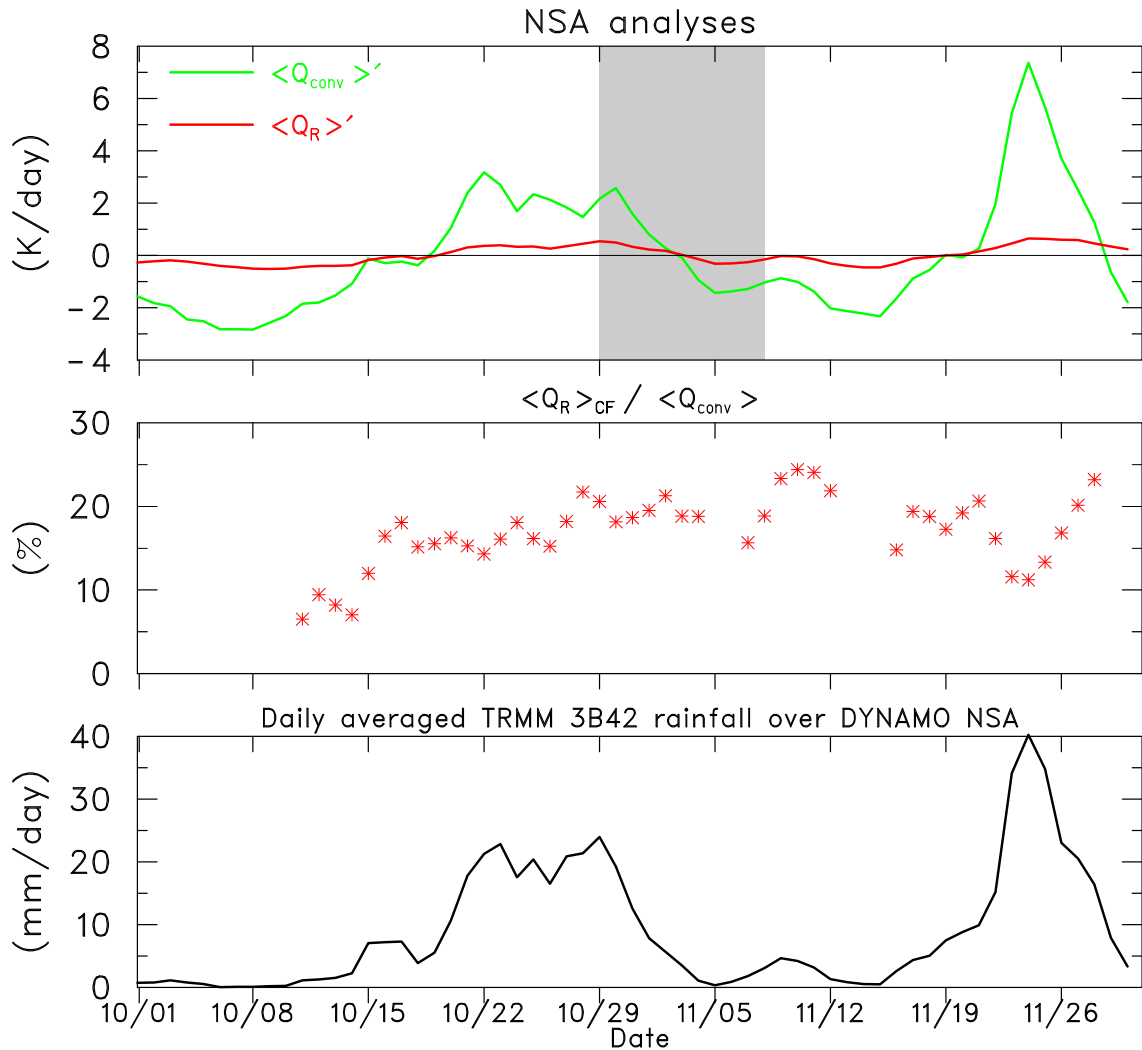
966 FIG. 10. (left) Time series of daily-averaged net radiative heating rate (K day⁻¹) at Gan Island from PNNL
 967 CombRet product and (right) mean profiles of shortwave (SW), longwave (LW) and net radiative heating rates
 968 for 10 October – 31 December 2011.



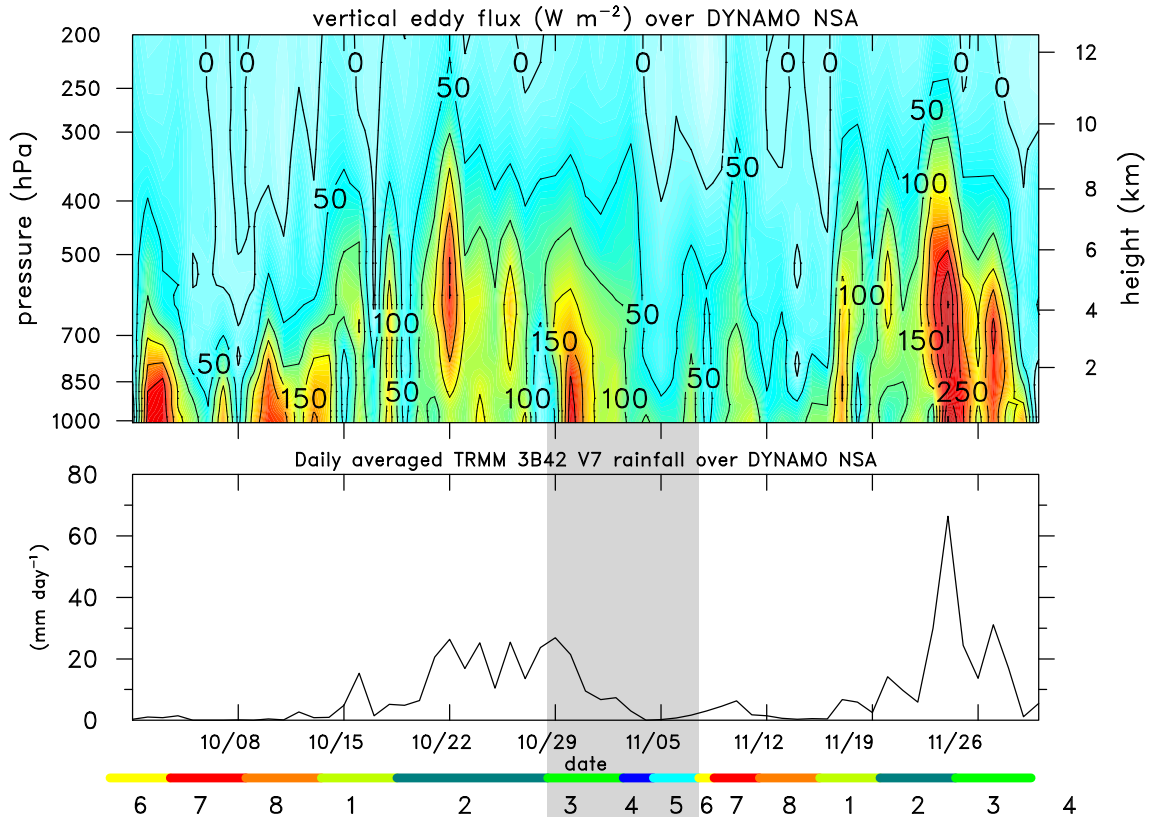
966 FIG. 11. SOP time series (3-day running mean filtered, daily-average values) of net radiative heating rate (K day^{-1}) from budgets and CERES product for array areas, and from PNNL CombRet product for Gan Island,
 967 day^{-1}) from budgets and CERES product for array areas, and from PNNL CombRet product for Gan Island,
 968 for (upper) NSA and (lower) SSA. Solid (dashed) black curves are $\langle Q_R \rangle$ with (without) inclusion of terms
 969 involving the effects of rain (see text). Numbers in parentheses are SOP-mean values. Light (dark) shading
 970 denotes periods of R/V *Revelle* (*Mirai*) port calls.



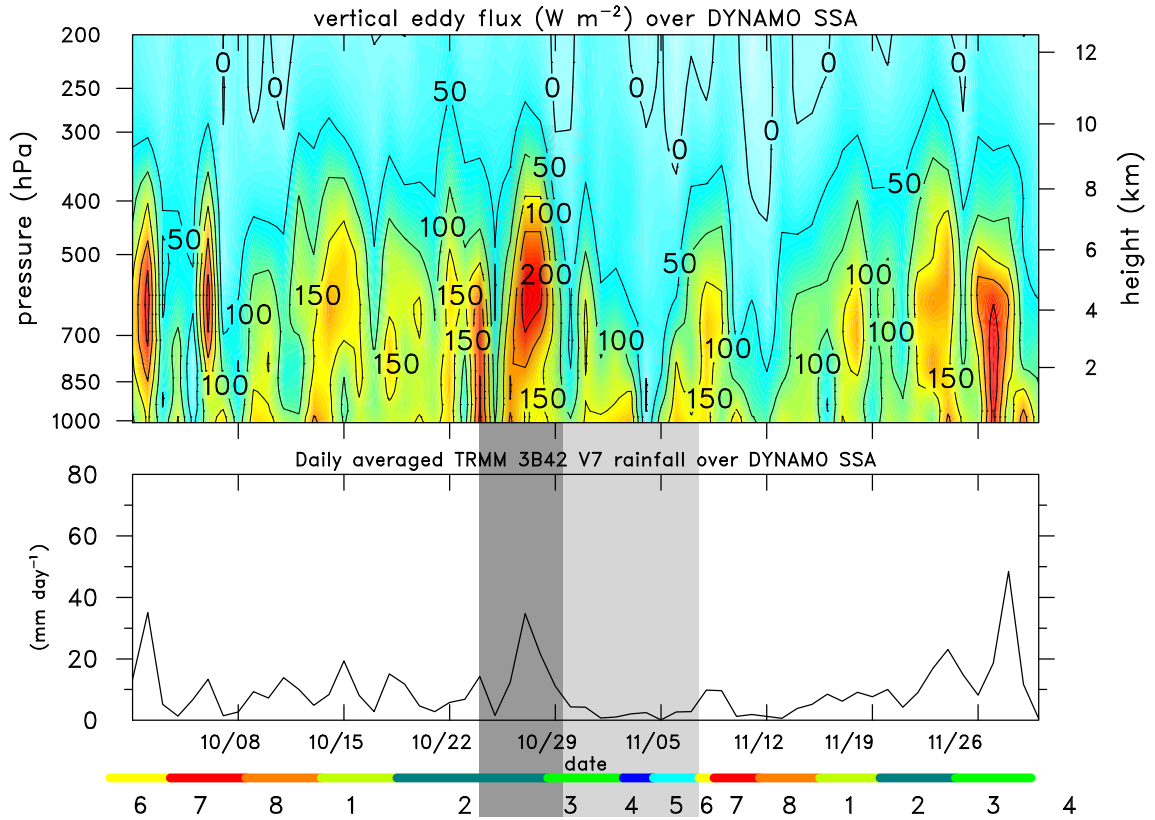
966 FIG. 12. October 1 – December 6 time series (3-day running mean filtered, daily-average values) of (upper)
 967 relative humidity (%; with respect to ice for $T < 0^\circ\text{C}$); (middle) $\langle Q_R \rangle$ from budgets (black) and CERES (red);
 968 and (lower) cloud fractional area from CERES for the following definitions of cloud layers: low ($p > 700$ hPa),
 969 med-low ($700 \text{ hPa} > p > 500 \text{ hPa}$), med-hi ($500 \text{ hPa} > p > 300 \text{ hPa}$), and high ($p < 300 \text{ hPa}$) for NSA. Shaded
 970 region denotes period when R/V *Reville* was off station. RMM index shown at bottom.



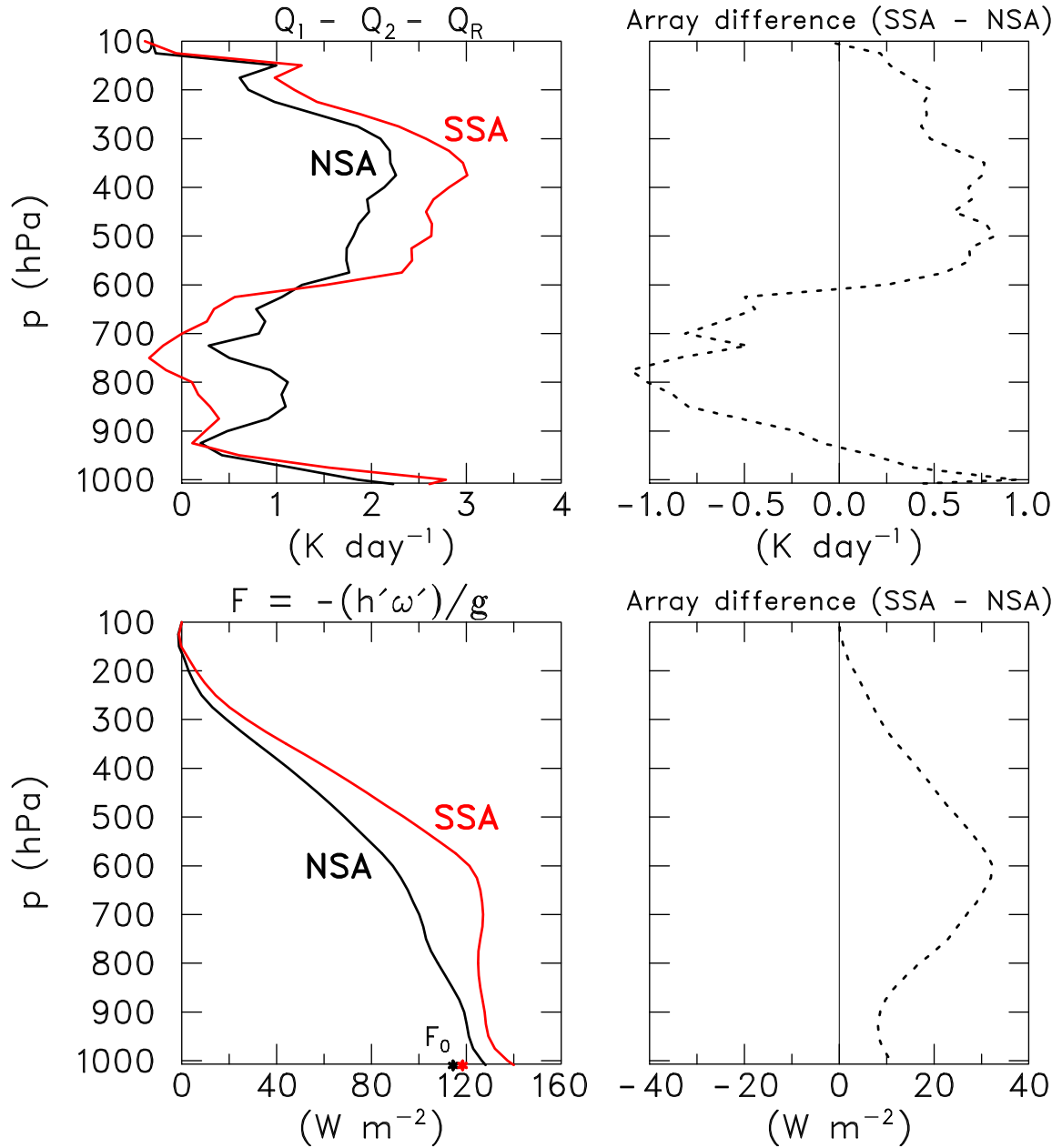
966 FIG. 13. (upper) Comparison of anomalies of CERES $\langle Q_R \rangle$ and convective heating $\langle Q_{conv} \rangle$ for NSA for
 967 DYNAMO SOP based on 3-day running mean filtered, daily-averaged values. (middle) Time series of ratio of
 968 cloud radiative forcing $\langle Q_R \rangle_{CF}$ to $\langle Q_{conv} \rangle$. Values plotted only when daily TRMM precipitation exceeded
 969 1 mm day^{-1} . (lower) TRMM 3B42 rainfall rate (mm day^{-1}) time series for NSA. Shaded region denotes period
 970 when R/V *Revelle* was off station.



966 FIG. 14. Time series of daily-average values of (upper) vertical eddy moist static energy flux F (contours: 50
 967 W m^{-2} intervals; shading denotes gradations between intervals) and (lower) TRMM 3B42v7 rainfall rate (mm
 968 day^{-1}) for NSA for DYNAMO SOP. Shaded region denotes period when R/V *Revelle* was off station. RMM
 969 index shown at bottom.



966 FIG. 15. As in Fig. 14, except for SSA. Dark and light vertical shaded bars indicate times when R/V *Mirai*
 967 and *Revelle*, respectively, were off station.



966 FIG. 16. (upper left) SOP-mean profiles of $Q_1 - Q_2 - Q_R$ (K day⁻¹) for NSA and SSA and (upper right) SSA
 967 minus NSA difference in those quantities. (lower left) F (W m⁻²) for NSA and SSA and (lower right) SSA
 968 minus NSA difference in F . Surface sensible plus latent heat flux (F_0) from TropFlux is indicated by asterisks
 969 on bottom lower-left axis for NSA (black) and SSA (red).